

Review

Lithium-Ion Batteries under the X-ray Lens: Resolving Challenges and Propelling Advancements

Mahdieh Samimi ^{1,*}, Mehran Saadabadi ²  and Hassan Hosseinlaghab ³¹ School of Electronic Engineering, Dublin City University, D09 W6Y4 Dublin, Ireland² Mechanical Engineering Department, Amirkabir University of Technology, Tehran 1591634311, Iran; mehransaadabadi@aut.ac.ir³ Independent Consultancy, D11 E4A6 Dublin, Ireland; gmhasanjanh@gmail.com

* Correspondence: m.samimi.86@gmail.com or mahdieh.samimi2@mail.dcu.ie

Abstract: The quest for high-performance lithium-ion batteries (LIBs) is at the forefront of energy storage research, necessitating a profound understanding of intricate processes like phase transformations and thermal runaway events. This review paper explores the pivotal role of X-ray spectroscopies in unraveling the mysteries embedded within LIBs, focusing on the utilization of advanced techniques for comprehensive insights. This explores recent advancements in in situ characterization tools, prominently featuring X-ray diffraction (XRD), X-ray tomography (XRT), and transmission X-ray microscopy (TXM). Each technique contributes to a comprehensive understanding of structure, morphology, chemistry, and kinetics in LIBs, offering a selective analysis that optimizes battery electrodes and enhances overall performance. The investigation commences by highlighting the indispensability of tracking phase transformations. Existing challenges in traditional methods, like X-ray absorption spectroscopy (XAS), become evident when faced with nanoscale inhomogeneities during the delithiation process. Recognizing this limitation, the review emphasizes the significance of advanced techniques featuring nanoscale resolution. These tools offer unprecedented insights into material structures and surface chemistry during LIB operation, empowering researchers to address the challenges posed by thermal runaway. Such insights prove critical in unraveling interfacial transport mechanisms and phase transformations, providing a roadmap for the development of safe and high-performance energy storage systems. The integration of X-ray spectroscopies not only enhances our understanding of fundamental processes within LIBs but also propels the development of safer, more efficient, and reliable energy storage solutions. In spite of those benefits, X-ray spectroscopies have some limitations in regard to studying LIBs, as referred to in this review.

Keywords: X-ray spectroscopy; lithium-ion batteries; SEI; degradation; thermal runaway; heterogeneity; cracks



Citation: Samimi, M.; Saadabadi, M.; Hosseinlaghab, H. Lithium-Ion Batteries under the X-ray Lens: Resolving Challenges and Propelling Advancements. *Quantum Beam Sci.* **2024**, *8*, 10. <https://doi.org/10.3390/qubs8020010>

Academic Editor: Shinji Kohara

Received: 9 January 2024

Revised: 17 March 2024

Accepted: 25 March 2024

Published: 27 March 2024



Copyright: © 2024 by the authors. Licensee MDPI, Basel, Switzerland. This article is an open access article distributed under the terms and conditions of the Creative Commons Attribution (CC BY) license (<https://creativecommons.org/licenses/by/4.0/>).

1. Introduction

Energy storage technologies have proven pivotal across a spectrum of applications, including fuel cells, batteries, and other energy storage devices. While fuel cells harness electrochemical reactions to generate electricity from fuels like hydrogen, batteries excel in storing energy in chemical form, with reversible reactions occurring during charging and discharging. Batteries, with their versatility and widespread use in portable electronics, grid energy storage, electric vehicles, and backup power systems, offer high energy density, rapid response times, and scalability, contributing significantly to the landscape of energy storage solutions [1].

Lithium-ion batteries (LIBs) are essential for portable electronics and sustainable energy solutions. Despite their widespread use, safety concerns arise, particularly during high charge rates and overcharging. Catastrophic failures due to thermal runaway, triggered by overcharge, underscore the need for risk reduction. In addition, thermal runaway in

batteries occurs when overcharging or internal short circuits lead to temperatures beyond manufacturer ratings. At a critical temperature, a chain of exothermic reactions triggers rapid self-heating, and without proper heat dissipation, the battery catastrophically fails, as characterized across various length scales from electrode microstructure to the entire cell and pack [2]. Understanding phase transitions, as well as the spatial and temporal dynamics of exothermic reactions within LIB components, is crucial for enhancing safety protocols, mitigating potential hazards, and enhancing overall battery development.

Increasing storage performance in systems like batteries involves optimizing several operational parameters, including electrolyte composition, temperature, and current density. Optimizing electrolyte composition involves selecting suitable solvents, salts, and additives to enhance ion conductivity, minimize internal resistance, and improve cycling stability [3]. For example, using high-conductivity solvents like ethylene carbonate (EC) or dimethyl carbonate (DMC) with lithium salts such as LiPF_6 can enhance ion mobility in lithium-ion batteries, thus improving their overall performance [4]. Additives like fluoroethylene carbonate (FEC) can also form stable passivation layers on electrode surfaces, reducing side reactions and improving long-term cycling performance [5]. Current density refers to the amount of electrical current per unit area of electrode surface, and higher current densities usually result in faster charge/discharge rates but can also lead to increased internal resistance and heat generation [6]. Generally, higher temperatures increase ion mobility and electrode kinetics, leading to enhanced charge/discharge rates and overall performance. However, excessively high temperatures can accelerate side reactions, degrade electrolytes, and reduce the lifespan of the device. Therefore, maintaining an optimal operating temperature range is crucial for maximizing storage performance while ensuring device longevity [7]. Advanced thermal management systems, such as liquid cooling or phase change materials, can help regulate temperature within the desired range [8,9]. Optimizing current density involves balancing the need for rapid energy transfer with the limitations imposed by electrode/electrolyte interface kinetics. Advanced electrode designs, such as nanostructured materials or porous architectures, can mitigate the effects of high current densities by reducing diffusion distances and enhancing surface area [10]. Control strategies, such as pulse charging/discharging or current ramping, can also help manage current density variations during operation [11].

Advanced characterization techniques are required for exploring LIBs from macro to micro and from thermodynamics to kinetics [12,13].

Tracking phase transformations in LIBs is vital for resolving debates and understanding fundamental mechanisms within the delithiation process for olivine-type cathodes (which embodying a two-phase mechanism) like LiFePO_4 . This process is key to improving battery performance, especially at large scales, by avoiding pitfalls related to averaging methods, such as traditional X-ray absorption spectroscopy [14] and revealing inhomogeneity behaviors. Overall, this knowledge is crucial for optimizing battery designs and advancing energy storage technologies for diverse applications [15].

Lithium-ion batteries store lithium ions using different methods, such as intercalation, conversion, alloying reactions, surface storage, hybrid mechanisms, and chemical redox reactions. Intercalation, the more common method, involves lithium ions lodging in the crystal structure of the electrode material. Conversion, on the other hand, involves lithium ions reacting with the electrode material to form a new compound. Unlike intercalation, conversion reactions involve Li-substituting cation species, often transition metals, resulting in displacement reactions due to the absence of empty sites for Li ions in the crystal structures. Conversion-type electrodes are known for their high theoretical specific capacities; however, this conversion process can cause larger volume changes in electrodes compared to intercalation. Irreversible electrochemical reactions in transition metal oxides (TMOs) cause capacity fading, requiring detailed understanding through X-ray characterization [16]. Alloying reactions present another alternative, offering high specific capacities through the formation of alloys with the electrode material. This can result in high-energy densities, but the pronounced volume changes during charge and discharge cycles can lead

to mechanical degradation and reduced cycle life compared to intercalation-based batteries [17]. Surface storage provides a different approach that involves the adsorption and desorption of lithium ions directly onto the surface of the electrode material. This allows for fast lithium-ion transport and high-power densities, making it suitable for applications requiring rapid charge and discharge rates. However, surface storage typically offers lower energy densities compared to intercalation or conversion, limiting its suitability for certain applications [18]. Hybrid mechanisms combine elements of different storage methods to achieve a balance between high specific capacities, fast charge/discharge rates, and long cycle life. While offering flexibility in optimizing performance and stability, hybrid mechanisms require sophisticated electrode design and material engineering, which can increase manufacturing costs [19]. Chemical redox reactions introduce yet another avenue, offering tunable redox potentials and the potential for unique applications and performance enhancements. However, achieving stability and long-term performance with chemical redox reactions requires careful selection and designing of electrode materials [20].

The choice of anode and cathode materials affects the storage mechanism. Common cathode materials like lithium cobalt oxide, lithium iron phosphate, and lithium nickel manganese cobalt oxide primarily use intercalation. Meanwhile, common anode materials, like graphite and lithium titanate, also use intercalation, while silicon undergoes conversion [21].

The structure and morphology of the electrode material has a significant impact on how lithium-ion batteries store and release energy. Materials with a high surface area, like zero-dimensional nanoparticles and two-dimensional nanosheets, can store more lithium ions [17,22]. Porous structures in three dimensions also help by allowing the electrolyte to penetrate deeper into the electrode, which improves capacity [23]. Additionally, one-dimensional nanostructures provide efficient paths for lithium ions to move, which facilitates rapid charging and discharging [24]. However, complex pathways or tortuosity within three-dimensional structures can slow down lithium-ion diffusion and hinder performance [25]. They can achieve this by tailoring the structure of the electrode material to optimize lithium-ion transport, maximize the number of active sites, and accommodate volume changes. This will lead to lithium-ion batteries with exceptional capacity, rate capability, and cycling stability, paving the way for the development of next-generation energy storage solutions for a sustainable future.

In addition, high-performance lithium-ion batteries (LIBs) rely heavily on the properties of their electrode materials. These properties, in turn, are significantly influenced by the chosen synthesis method. Therefore, it is important to explore how various synthesis techniques impact the structure and storage capacity of LIB electrodes.

Synthesis methods offer broader control over the microstructure and chemical composition of electrode materials. Techniques like sol-gel processing [26] or spray-drying [27] enable the fabrication of materials with tailored properties. Sol-gel processes, in particular, facilitate the transformation of small molecules into solid materials, offering precise control over porosity and elemental distribution. This control often translates to enhanced efficiency and storage capacity of electrode materials [26]. Similarly, synthesis methods, like solid-state reactions [28] or vapor deposition [29], can be tailored to manipulate the phases present in the final material, potentially impacting its capacity and cyclability. Hydrothermal synthesis (which involves the reaction of precursor materials in an aqueous solution under high-temperature and high-pressure conditions) and ball milling (which involves grinding precursor materials together with balls in a high-energy mill) are two methods for creating particles with a controlled size, porosity, and grain boundaries [30,31]. These properties influence how the material handles stress and strain during lithium-ion insertion/removal cycles, ultimately affecting capacity and cyclability.

Synthesis methods are crucial for lithium metal anodes and key to achieving high-energy density LIBs. Techniques like lithium foil deposition or stripping address challenges like dendrite growth and volume changes during cycling, ultimately improving safety and cycle stability. Furthermore, dendritic copper current collectors mitigate these issues by

enhancing ion transfer and promoting cycle stability for long-term performance without short circuits [32]. Heat treatment also plays a role in synthesizing material and developing storage capacity. For instance, heat treatment of Co_3O_4 for LIB anodes improves storage capacity and lifespan by strengthening connections between electrode materials, facilitating better lithium movement [33]. In conclusion, the synthesis method plays a critical role in shaping the microstructure and morphology of LIB-electrode materials. By carefully selecting and optimizing these methods, researchers can create high-performance electrode materials that unlock the full potential of LIB technology.

Material categorization based on crystal structure is crucial for understanding the behavior of lithium-ion battery active materials, especially cathodes. The three following main categories shall be discussed: layered, spinel, and olivine. Layered structures, such as LiCoO_2 , create open spaces for lithium ions, facilitate smooth diffusion, and enable high capacity with fast charging/discharging. However, structural distortions during ion movement can lead to a sloping voltage profile. Spinel structures like LiMn_2O_4 form a three-dimensional network where lithium ions occupy tetrahedral and octahedral sites. Tetrahedral sites offer easier movement, resulting in a higher capacity at a specific voltage, while filling octahedral sites require more energy, leading to multiple voltage plateaus. Olivine structures, exemplified by LiFePO_4 and LiMnPO_4 , have MO_6 octahedra and PO_4 tetrahedra connected through corner-sharing networks, resulting in a densely packed structure with minimal distortions during lithium movement. Although diffusion may be slower, the constant energy requirements lead to a nearly flat voltage profile with a good capacity [34].

Crystal structure significantly influences lithium-ion movement within cathode materials, impacting capacity and charging/discharging mechanisms. Layered structures offer high capacity but may suffer from a sloping voltage profile, while spinel structures exhibit multiple plateaus due to distinct lithium-ion occupation sites. Olivine structures provide good capacity with a flat voltage profile [34].

Beyond crystal structure, the morphology of active materials (Co, Fe, Mn, and Ni) significantly influences their performance. By manipulating morphology, researchers can control surface area, electrolyte contact, and lithium-ion transport pathways. Active materials in lithium-ion battery (LIB) electrodes are categorized based on morphology, including zero-dimensional (0D), one-dimensional (1D), two-dimensional (2D) and three-dimensional (3D) structures. Zero-dimensional (0D) nanoparticles (NPs) like LiFePO_4 and Si-NPs offer high surface areas, aiding electrolyte contact and Li-ion diffusion [35,36]. One-dimensional (1D) structures, such as nanorods and nanotubes, provide direct Li-ion transport paths, exemplified by Co_3O_4 nanorods and TiO_2 nanotubes [37,38]. Two-dimensional (2D) nanosheets and graphene offer large surface areas like 0D NPs while potentially addressing volume change issues. MoS_2 nanosheets are notable examples [39]. Three-dimensional (3D) hierarchically porous structures, like sphere LiNiCoMnO_2 (NCM), combine high surface areas, electrolyte penetration, and mechanical integrity [40].

Morphology influences capacity and storage mechanisms in LIBs. High surface area morphologies (0D NPs, 2D nanosheets) offer more active sites, potentially boosting theoretical capacities. Porous structures (3D) enhance electrolyte penetration, improving active material utilization. Direct Li-ion pathways in 1D nanostructures enhance charge/discharge rates, while tortuosity in 3D structures may hinder diffusion [41,42]. Understanding these relationships informs the design of LIB electrodes for improved performance.

Utilizing advanced techniques with nanoscale resolution provides direct evidence of dynamic phase changes, validating theoretical models and guiding the development of high-rate battery technology.

These advanced techniques include in situ and ex situ approaches. In situ/operando approaches offer crucial advantages over ex situ characterization in lithium-ion battery (LIB) research. In situ techniques provide real-time insights by instantly probing reactions at specific locations, ensuring better reliability and higher precision in data analysis. Continuous in operando measurements monitor electrochemical, physical, and chemical

processes on a single sample, eliminating the need for multiple samples and offering closer-to-real-time operational information. This methodology is particularly advantageous when employing X-ray techniques due to their compatibility with in situ/operando studies. This compatibility is vital for LIB research as it allows for real-time investigation of material transformations and chemical reactions occurring within the battery during operation [6]. X-rays, as non-destructive tools, enable the study of the battery without causing permanent damage to the sample, allowing for continuous monitoring throughout the experiment [8]. Additionally, their deep penetration allows for probing the bulk of the battery compared to other techniques like electron microscopy, providing insights into bulk material behavior. This methodology enables the investigation of non-equilibrium or fast-transient processes, detecting short-lived intermediate states not captured by ex situ methods. In situ approaches prevent contamination and irreversible changes in highly reactive samples during preparation and transfer, enhancing the reliability of identifying true reaction products. Advanced in situ/operando synchrotron-based experiments significantly contribute to understanding complex reaction mechanisms in LIBs [43].

The operando method enables the observation of dynamic occurrences like thermal runaway, allowing for a comprehensive understanding of crucial degradation mechanisms. This includes phenomena like delamination caused by gas production, pulverization of the electrode layer, and the structural separation of islands [44].

In recent years, significant advancements in in situ characterization tools have enhanced the understanding of material structures and surface chemistry in operating conditions. In situ X-ray absorption spectroscopy (XAS) stands out for revealing the atomic and electronic structure of active host metals during operation. Figure 1 provides a summary of crucial in situ X-ray techniques, their spatial resolutions, and detection objectives in batteries, enabling selective analysis of structure, morphology, chemistry, and kinetics. These techniques, including X-ray diffraction (XRD), XAS, transmission X-ray microscopy (TXM), and X-ray tomography (XRT), contribute to comprehensive studies, optimizing battery electrodes and enhancing overall battery performance through insights into phase transformations and electrode deformation [45].

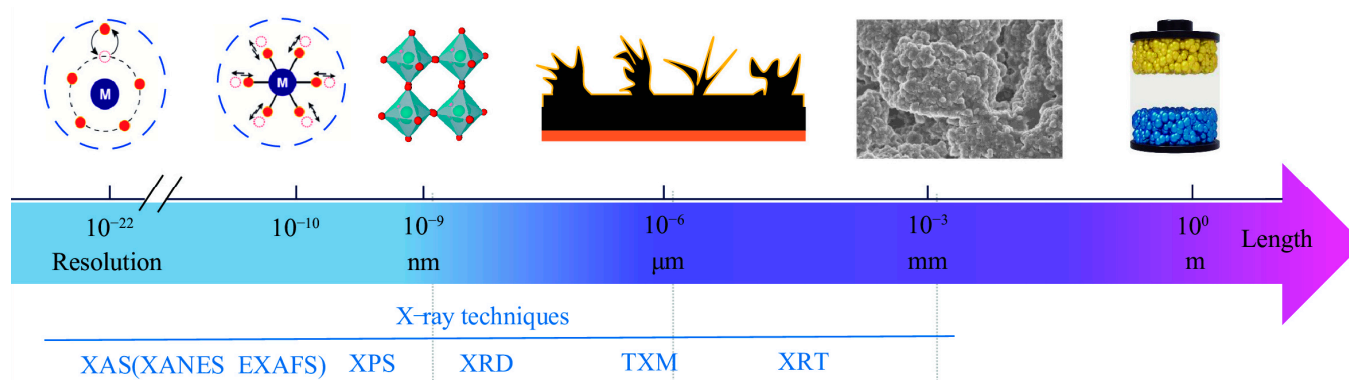


Figure 1. Primary in situ X-ray characterization methods, along with their spatial resolution scales and associated detection objectives in battery research, include X-ray absorption near-edge structure (XANES), extended X-ray absorption fine structure (EXAFS), X-ray photoelectron spectroscopy (XPS), transmission X-ray microscopy (TXM), and X-ray tomography (XRT) [45].

1.1. X-ray Tomography (XRT)

XRT utilizes attenuation-based imaging at synchrotrons, employing a collimated X-ray beam in a rotational setup (Figure 2a). A sample, placed on a rotating stage, undergoes X-ray penetration, with attenuated rays being converted into visible light by a scintillator and captured by a camera. Sequential projections at varying angles create a dataset for tomographic reconstruction, revealing the internal structure in 3D. Figure 2b illustrates the rotating sample, emphasizing the distinct attenuation of X-rays by different phases.

XRT employs mathematical principles, such as the Fourier slice theorem, for efficient reconstruction from 2D projections, enabling detailed material characterization [46].

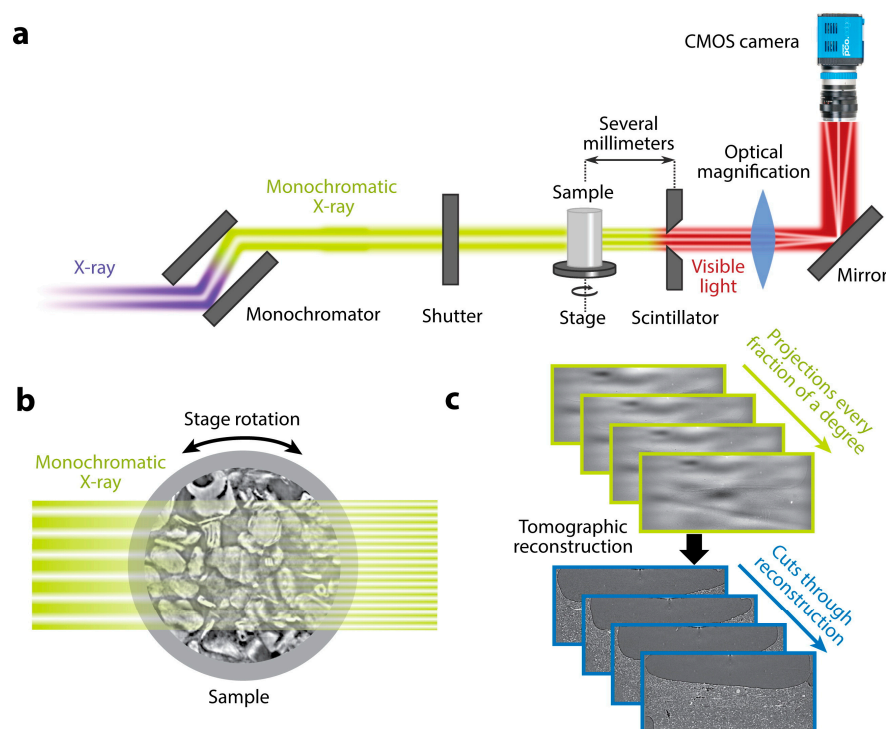


Figure 2. Tomography concept: (a) Diagram depicting a conventional experimental arrangement for attenuation contrast. Coherent X-rays penetrate a sample fixed on a rotating stage. The transmitted beam transforms into visible light via a scintillator and the resultant image is optically enlarged and documented using a CMOS camera. Sketch provided by Simon Muller. (b) Visualization of X-rays permeating the revolving sample. (c) Projections acquired at diverse angles are re-constructed into a 3D dataset, depicted as virtual cross-sections [6].

XRT is a valuable tool for studying LIBs at various scales (Figure 3). At the cell level, it scrutinizes key design factors, such as anode and cathode dimensions, packing density, and cell alignment, while also detecting macroscopic issues like islanding. Moreover, it enables precise analysis of electrode microstructures, quantifying particle size, tortuosity, and volume fraction. Additionally, various techniques, including ex situ, in situ, and operando methods, can be seamlessly integrated with X-ray computed tomography to characterize battery materials [44].

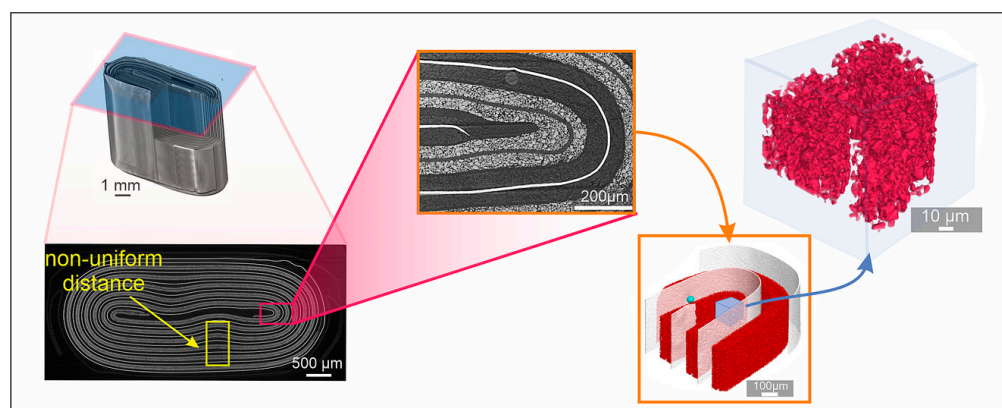


Figure 3. Multi scale applications of XRT for studying LIBs [47].

Assembled cells for electrochemical storage testing in lithium-ion batteries are classified based on the type of electrode configuration, which encompasses the preparation of working electrodes, the selection of reference and counter electrodes, and whether the cell is configured as a three- or two-electrode system. Each aspect of the electrode configuration is meticulously chosen to facilitate accurate and reliable measurement of electrochemical performance during testing [48].

The working electrode typically comprises the active material coated onto a conductive substrate, such as copper foil for cathodes or graphite for anodes. Cathodes are commonly prepared by blending the active material (e.g., lithium cobalt oxide, lithium iron phosphate) with conductive additives and a binder before applying the slurry onto a current collector. Anodes undergo a similar process, with the active material (e.g., graphite, silicon) coated onto a current collector. The method of electrode preparation may vary based on the specific material and testing requirements [49].

In lithium-ion battery testing, the reference electrode usually consists of a stable electrode material with a known potential, such as a lithium metal foil or a lithium-ion intercalation electrode. Meanwhile, the counter electrode complements the circuit and is often composed of a material similar to the working electrode (e.g., lithium cobalt oxide for cathodes, graphite for anodes) [50]. Three-electrode cells comprise a working electrode, a reference electrode, and a counter electrode, allowing for precise control of potential and measurement of currents during electrochemical cycling [51]. Conversely, two-electrode cells amalgamate the working and counter electrodes into a single electrode, streamlining the cell setup but constraining control over the potential at the working electrode. The decision between three and two-electrode cells hinges on specific testing requirements, encompassing the desired level of control and the complexity of the electrochemical system under investigation. The selection of reference and counter electrodes aims to ensure stable electrochemical behavior and minimize interference with the measurement of the working electrode [50].

Kodama et al. [52] proposes a high-resolution method for measuring the 3D material distribution in an All-Solid-State Lithium-Ion Battery (ASSLiB) cathode using synchrotron radiation X-ray nano-computed tomography (CT) imaging. The experiments with high-energy, 20 keV X-rays successfully achieved a 40 nm voxel with minimal artifacts. Material identification using conventional CT value methods faced challenges due to small differences in X-ray absorption coefficients. However, the study overcame this using deep learning with a customized U-net (A type of convolutional neural network), enabling efficient material identification and segmentation of nano-CT images at high speed and low computational cost, making it applicable for high-resolution material distribution measurements in all-solid-state batteries. A raw X-ray nano-CT image using 12 keV X-rays (Figure 4a) depicts challenges in material identification due to the overlapping CT values of a solid electrolyte (SE) and void, resulting in ring artifacts. Figure 4b shows improved X-ray nano-CT images at 20 keV, where high signal-to-noise ratio and clear identification of materials (NCM, SE, and void) are achieved. Figure 4c presents relative CT values, indicating the difficulty of material identification with 12 keV X-rays and the improved distinguishability of materials with 20 keV X-rays.

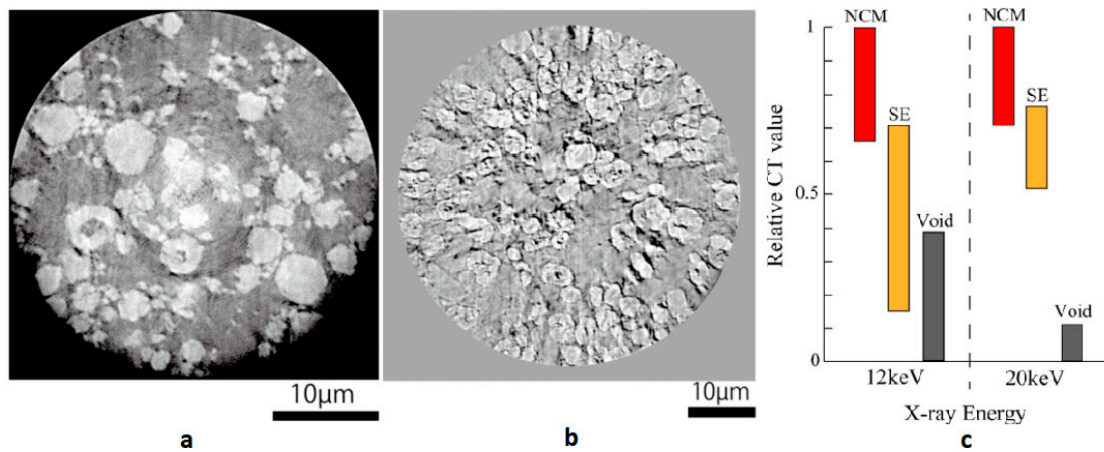


Figure 4. (a) X-ray nano-CT image acquired with 12 keV X-rays. (b) X-ray nano-CT image obtained using 20 keV X-rays. (c) Relative CT values in the nano-CT image for each material [52].

1.2. X-ray Diffraction (XRD)

XRD is pivotal for LIB analysis, tracking structural changes during charge/discharge. Synchrotron facilities enhance in situ studies, offering advantages like time resolution. Figure 5 illustrates XRD’s principles: diffraction patterns reveal the atomic structure while Bragg’s law defines scattering conditions. In situ XRD cells demand X-ray transparency, prevention of electrolyte leakage with a seal and uniform compression for optimal performance. Materials like beryllium, glassy carbon, and thin metal foils are common window choices, each with pros and cons. XRD can operate in reflection or transmission modes, with innovative designs overcoming challenges to enable detailed studies [53].

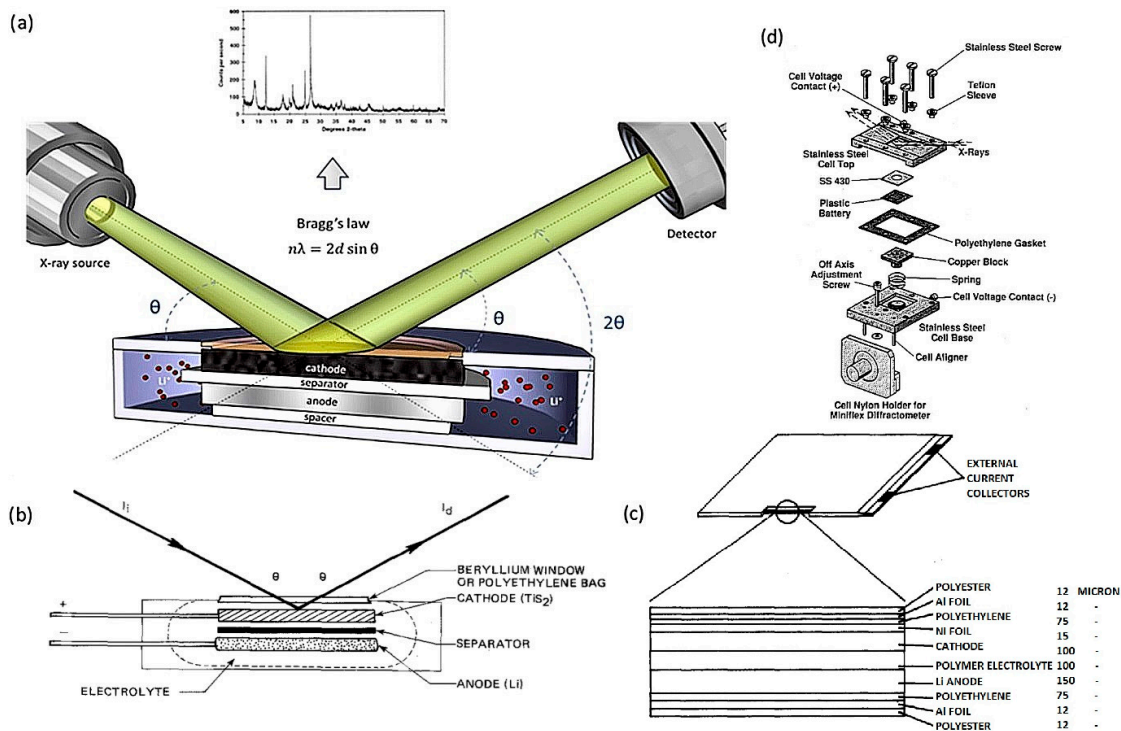


Figure 5. (a) schematic of XRD working principle with an example of the obtained pattern; (b) schematic of the in situ cell developed by Chianelli and co-authors; (c) schematic of the first developed in situ cell for transmission analysis; (d) representation of the in situ cell developed by Amatucci and co-workers [53].

Wilson et al. [54] conduct Operando XRD on LiFePO_4 during electrochemical cycling in a coin cell with a Kapton window. The findings, consistent with prior research, confirm the dual-phase solid solution behavior during lithium extraction from LiFePO_4 . The voltage profile of LiFePO_4 during the first charge and discharge cycles is illustrated in Figure 6a, while Figure 6b presents the corresponding XRD patterns of a LiFePO_4 cell with a Kapton window throughout the same cycles. Figure 6c displays more focused XRD patterns within the 10 to 15 degrees 2θ range. Certain Bragg peaks in the full profiles, including those attributed to carbon black (at $9^\circ 2\theta$), aluminum current collector (at 15.8 and $22.5^\circ 2\theta$), and steel casing (at 15.4 and $17.8^\circ 2\theta$), remain constant irrespective of cell charge state. Upon initiation of the charging process, the peaks corresponding to LiFePO_4 shift towards higher scattering angles, signifying a reduction in the unit cell size due to the extraction of Li from the material. This phenomenon is clearly demonstrated by the prominent 311 reflection in Figure 6c. The reverse behaviors are seen for the discharge process.

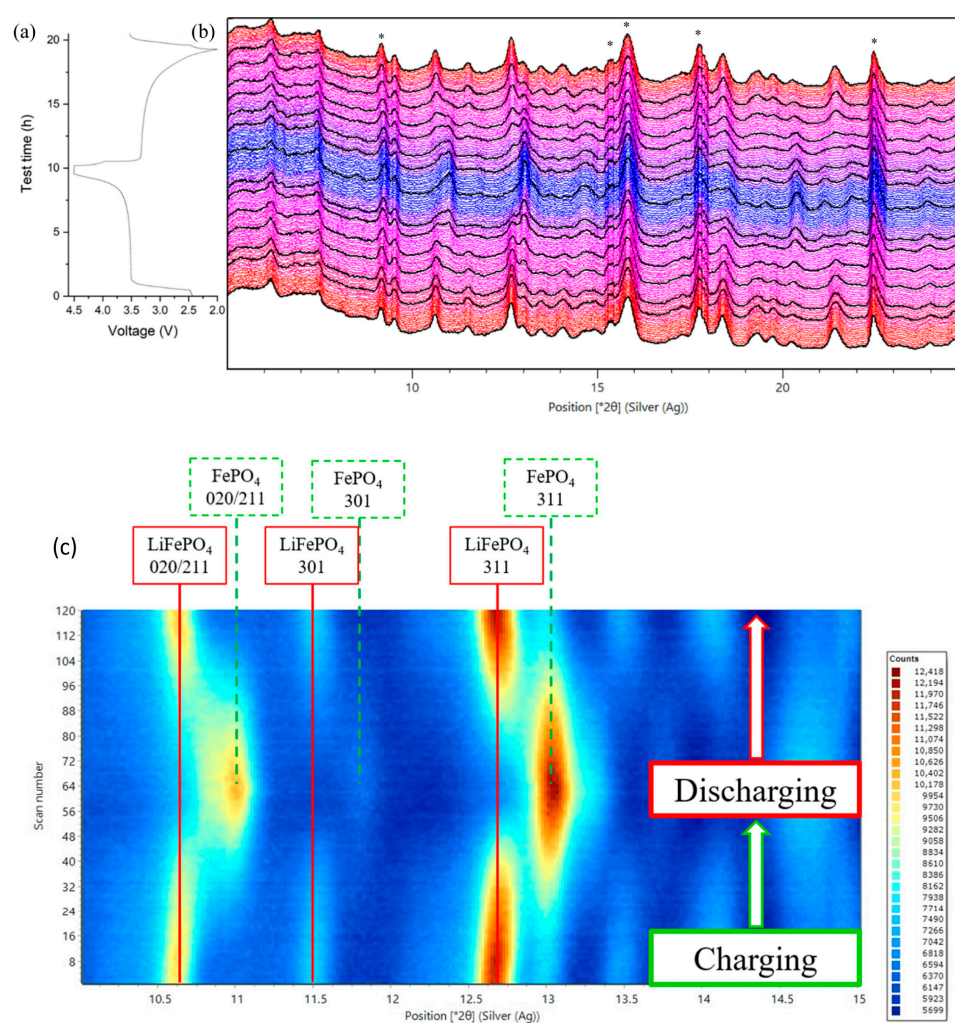


Figure 6. (a) The LiFePO_4 voltage profile in the initial charge and discharge cycles and (b) the XRD patterns of the Kapton cell throughout the first charging and discharging phases. All peaks associated with inactive material are specifically marked *. (c) Contour representation of diffraction peak intensities for Bragg reflections in LiFePO_4 and FePO_4 throughout the initial charging and discharging cycle [54].

1.3. X-ray Absorption Spectroscopy (XAS)

XAS plays a significant role in characterizing energy storage materials like LIBs. That investigates the absorption of X-rays by a material as a function of energy and provides

information about the electronic and local structural properties of elements in the sample. In particular, X-ray absorption near edge spectroscopy (XANES) and extended X-ray absorption fine structure (EXAFS) are crucial components of XAS. XANES provides insights into the geometrical structure and effective charge of the metal center, with the edge position indicating changes in the formal valence of the photo absorber. Pre-edge structures, observed in transition metal K-edges (K-edge refers to the energy threshold in XAS, indicating the ionization of inner-shell electrons of a specific element), offer valuable probes for geometry, especially in assessing geometrical distortions. On the other hand, EXAFS investigates the short-range structural information, revealing distances and coordination numbers around the selected atomic species. The oscillations in the EXAFS spectrum result from quantum-mechanical interference of the photoelectron scattered by neighboring atoms. Through advanced data analysis, including fitting procedures, the EXAFS technique enables the determination of structural parameters and coordination numbers. These XAS techniques, applied ex situ, in situ, or operando, contribute significantly to understanding the electrochemical mechanisms and stability of energy storage materials, thereby aiding the development of advanced batteries [55]. The X-ray absorption process involves photoelectron emission, influencing the absorption coefficient. Figure 7 illustrates the quantum-mechanical interference during this process. In isolated atoms (Figure 7a,c), emitted photoelectrons form spherical waves. In coordinated atoms (Figure 7b,d), neighboring atoms reflect the photoelectron back to the absorbing atom, creating oscillations in the X-ray absorption coefficient. This phenomenon, known as EXAFS, provides local structural information. The photoelectron's finite lifetime and decay over time and distance limit probing long-range distances. This mechanism is absent in isolated atoms, resulting in a featureless X-ray absorption edge (Figure 7c) [56].

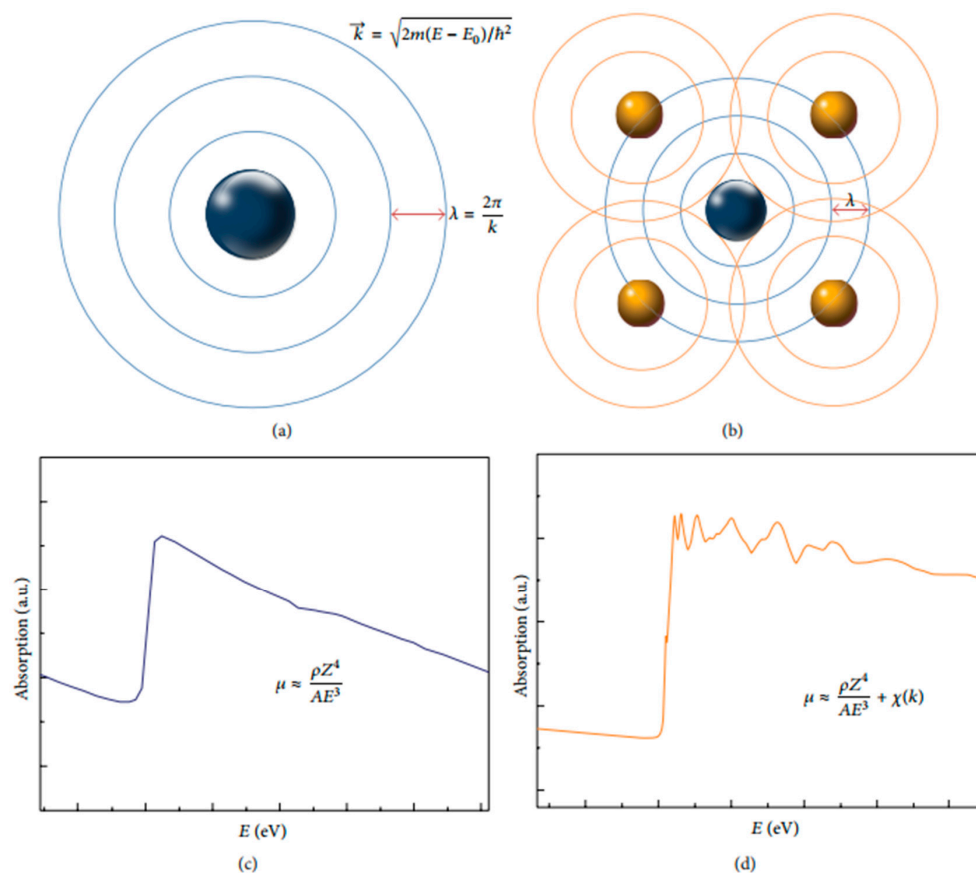


Figure 7. The release of a photoelectron from an individual (a,c) and a coordinated (b,d) atom. In the latter case, the absorption coefficient recorded at the central atom threshold displays intricate details attributed to the existence of surrounding atoms [56].

1.4. X-ray Photoemission or Photoelectron Spectroscopy (XPS)

The X-ray photoelectron spectroscopy (XPS) is a powerful tool for understanding and addressing challenges in energy storage devices, specifically Redox-flow batteries like LIB. As a surface-sensitive technique analyzes the composition and chemical state of the elements on the surface of a material, it is often used to study the solid–electrolyte interface (SEI) in LIBs. SEI is a thin layer that forms on the surface of the electrodes in LIBs during initial charging and discharging cycles. It results from the electrochemical reduction in the electrolyte and consists of lithium salts, organic compounds, and byproducts. The SEI serves critical functions, including passivation to prevent further electrolyte decomposition, facilitation of Li^+ transport while blocking electrons, and ensuring continued electrochemical stability. Analyzing the SEI is crucial for understanding long-term battery performance and addressing capacity loss and safety concerns [57]. XPS explores how to identify poisoning components of the SEI layers in LIBs, demonstrating that manipulating the lithium salt chemistry can extend the operating lifetime. An in situ XPS setup (depicted in Figure 8) was developed to analyze SEI layer formation in a model Li-S battery system during charge/discharge cycles. The setup utilizes Li metal and graphite foil as the anode and cathode, respectively, with an ionic liquid electrolyte. The paper concludes that in situ XPS and imaging provide deep insights into SEI layer formation, offering a valuable tool for reliability testing and understanding the electrochemical stability of commercial battery materials for next-generation advancements [58].

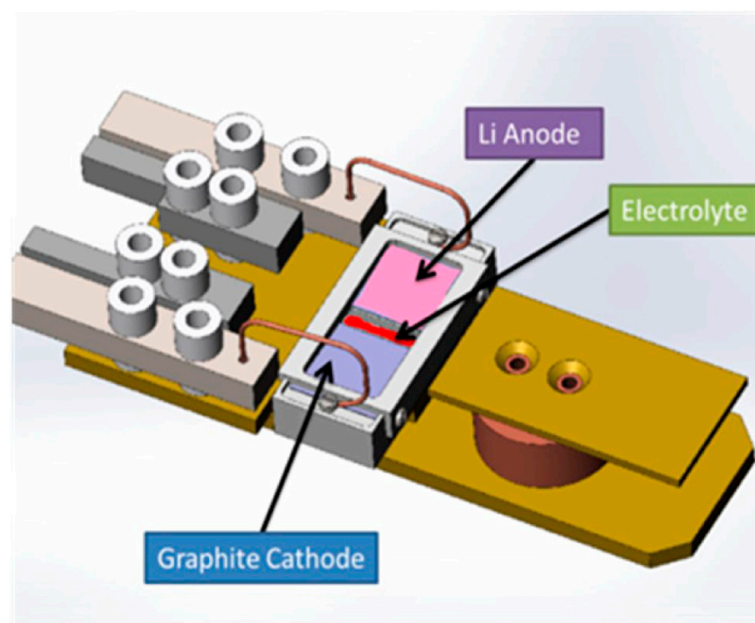


Figure 8. The XPS sample holder designed for battery cycling and in situ XPS characterization, as adapted from [59].

X-ray photoelectron spectroscopy (XPS) is a crucial technique in surface and materials science for chemical bonding determination, relying on a calibrated binding energy (BE) scale. The operational principles of XPS involve the photoelectric effect, where electrons are emitted from surfaces irradiated by light, with emitted electron energy dependent on incident photon energy. Figure 9 illustrates the schematic setup for XPS experiments, depicting the photon irradiation, photoelectric effect, and electron analysis in the spectrometer forming the XPS spectra [60].

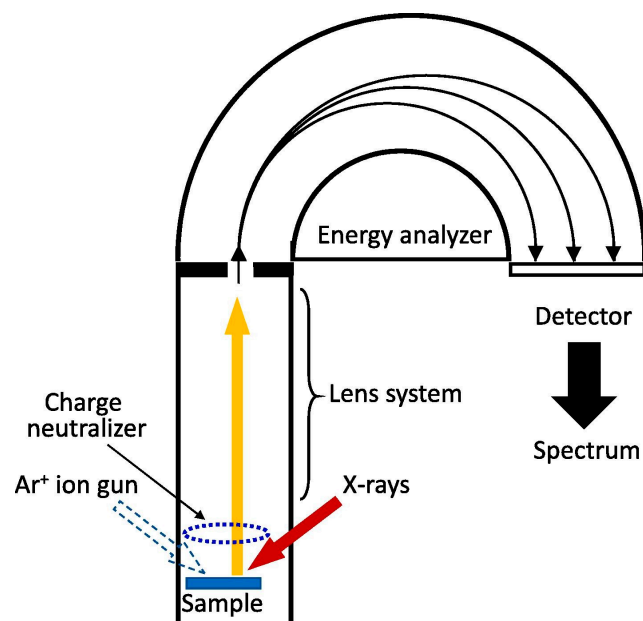


Figure 9. A diagrammatic representation depicting the photoelectron spectrometer featuring a hemispherical electron energy analyzer [60].

1.5. Transmission X-ray Microscopy (TXM)

The TXM technique, crucial for studying complex systems like batteries, employs high-penetration X-rays to investigate internal structures in bulk materials. Figure 10 illustrates the setup of a TXM, essential for studying hierarchical structures in complex systems like batteries. The TXM comprises an X-ray condenser, Fresnel zone plate (FZP) lens, and an X-ray detector. The FZP lens, with concentric zone structures, magnifies the X-ray transmission image, which is then captured by a scintillator and optical detector. The system's spatial resolution, ranging from tens to over a hundred nanometers, depends on the condenser, FZP lens, and detector properties. Operating in X-ray Absorption Spectroscopy (XAS) mode, the TXM scans the sample at different energy points, revealing the chemical state and local structure configuration. Figure 10 emphasizes the TXM's role in providing high spatial resolution, allowing for the visualization and quantification of redox events in battery materials, which is crucial for understanding their dynamic processes and heterogeneity. The figure showcases the key components instrumental in achieving these capabilities [61].

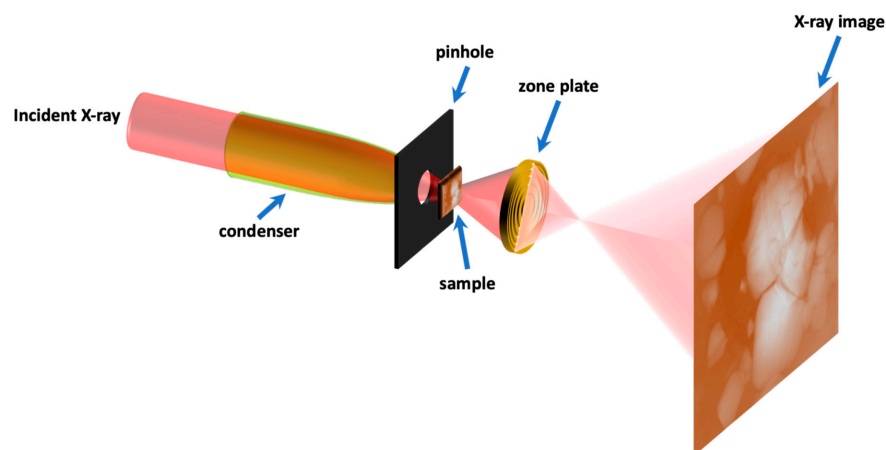


Figure 10. Configuration of TXM, where the X-ray transmission images of the sample are captured using an X-ray imaging detector (not depicted) [61].

Choi et al. [62] study lithium (Li) metal electrodeposition in high-energy-density batteries using in situ X-ray microscopy. Figure 11 depicts operando imaging during Li electrodeposition under controlled conditions. Initially, nucleation sites are randomly distributed on the Li surface. However, operando imaging reveals that the deposited Li mass, which appears grainy, propagates laterally along the electrode rather than perpendicular to it. The boundary between the pristine surface and the deposited Li moves laterally, filling the field of view over time. This observation challenges the conventional understanding of Li deposition mechanisms. The ability to distinguish lateral growth through operando imaging is crucial, providing insights into the impact of SEI resistivity and separator design on Li metal growth. The study underscores the significance of in situ/operando techniques for understanding and mitigating challenges in practical Li metal battery applications.

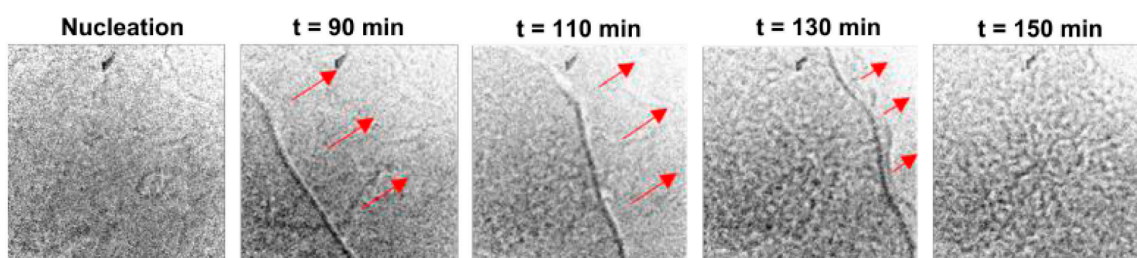


Figure 11. Chosen 2D X-ray images ($65\ \mu\text{m} \times 65\ \mu\text{m}$) depict the lithium metal anode captured through operando imaging under controlled settings ($1\ \text{mA cm}^{-2}$, $25\ ^\circ\text{C}$, using $1.2\ \text{M LiPF}_6$ in EC/DEC and Celgard 2400) [62].

2. Discussion: Different Degradation Mechanisms of LIBs Observed by X-ray Spectroscopies

2.1. Solid Electrolyte Interphase (SEI) Formation

The challenges in solid–solid interfaces involve both physical and chemical aspects. Physical challenges include point contact limitations between electrolytes and electrodes, leading to restricted ionic transport, with volume changes causing contact failure during battery cycling. Chemical challenges focus on side reactions between electrolyte and electrodes, reducing stability and increasing interfacial resistance. Key interfaces include cathode–electrolyte, anode–electrolyte, and interparticle interfaces, each presenting distinct issues such as resistive interphases, Li dendrite growth, and contact loss due to volume variations. Experimental evidence through microscopy, chemical analysis, and electrochemical characterization is essential to addressing these challenges despite theoretical insights into solid–solid interfaces, as observed in Figure 12 [63].

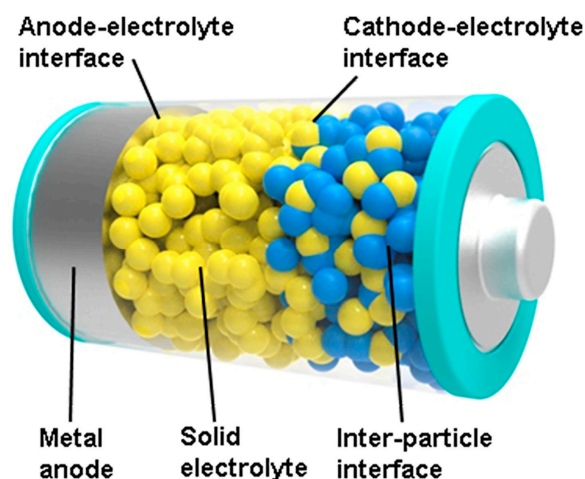


Figure 12. Various Interfaces in Solid-State Battery Systems [63].

The SEI's significance lies in its role as a passivating layer, preventing continuous reduction in an electrolyte while allowing ion diffusion. The complexity of the SEI composition, influenced by electrode material and electrolyte, necessitates a comprehensive understanding for advancements in battery technology. Figure 13 illustrates the ideal properties of the SEI [64].

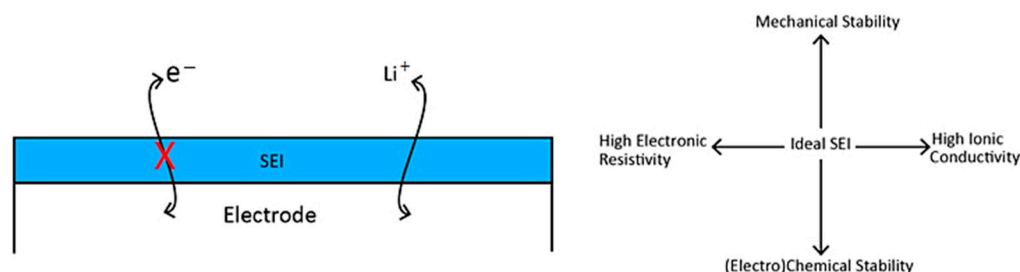


Figure 13. A visual representation illustrating the qualities of an optimal SEI includes such attributes as elevated electronic resistivity, lithium ion conductivity, mechanical durability, electrochemical resilience, and chemical stability. Additionally, the desired SEI should exhibit uniformity and compactness to mitigate fluctuations in lithiation, which may otherwise induce stress in both the SEI and the electrode [64].

Swallow et al. [65] employed operando soft X-ray absorption spectroscopy (sXAS) in total electron yield mode to investigate the formation of the SEI on high-capacity amorphous silicon (a-Si) anodes in LIBs. The technique offers nanometer-scale interface sensitivity, revealing the sequential evolution of inorganic (LiF) and organic ($-(C=O) O^-$) components during electrochemical cycling. The addition of fluoroethylene carbonate (FEC) has been found to influence SEI formation, leading to improved cycling performance through rapid healing of SEI defects. The research provides valuable insights into electrode–electrolyte interphase mechanisms, offering potential advancements for enhancing the stability and performance of LIBs. Figure 14 illustrates the total electron yield –XAS (TEY-XAS) data, showcasing the evolution of the Oxygen K-edge (O K-edge) and Fluorine K-edge (F K-edge) spectra with and without FEC in the electrolyte. FEC delays SEI onset to higher potentials, observed at 1.0 V, in contrast to 0.6 V without FEC. LiF formation at elevated potentials suggests enhanced SEI stability. The study underscores the potential of FEC to passivate SEI defects, offering insights into improved cycle lives for silicon electrodes.

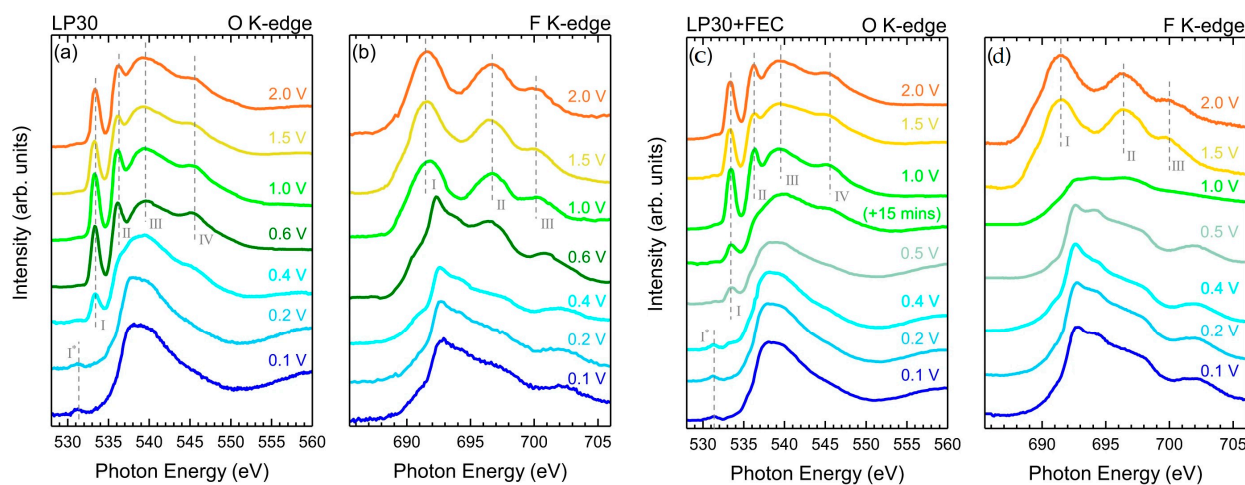


Figure 14. TEY XAS for (a) O K-edge and (b) F K-edge was conducted across various potentials (2.0 V to 0.1 V) in a cell with LP30 electrolyte without additives. Similarly, (c) O K-edge and (d) F K-edge were measured at different potentials in a cell with an LP30 electrolyte containing FEC as an additive. Notably, two O K-edge spectra at 1.0 V are shown, acquired 15 min apart [65].

In the investigation of solid-state lithium batteries, Narayanan et al. [66] present valuable insights into the evolution of the SEI at the lithium metal electrode interface using in situ X-ray photoemission spectroscopy (XPS). Figure 15a reveals Li plating behavior at different current densities, showing a faster formation of metallic Li at higher current densities. Figure 15b quantitatively supports this observation, indicating accelerated appearance of metallic Li layers at high current densities. Figure 15c,e detail SEI chemistry evolution, highlighting the formation of Li_2S and Li_3P -rich SEI at high current densities. Figure 15d,f provide quantitative evidence of SEI composition changes, emphasizing uniformity at high current densities. These findings provide insights into SEI kinetics, influencing the development of stable interfaces crucial for enhancing lithium plating efficiency in all-solid-state batteries.

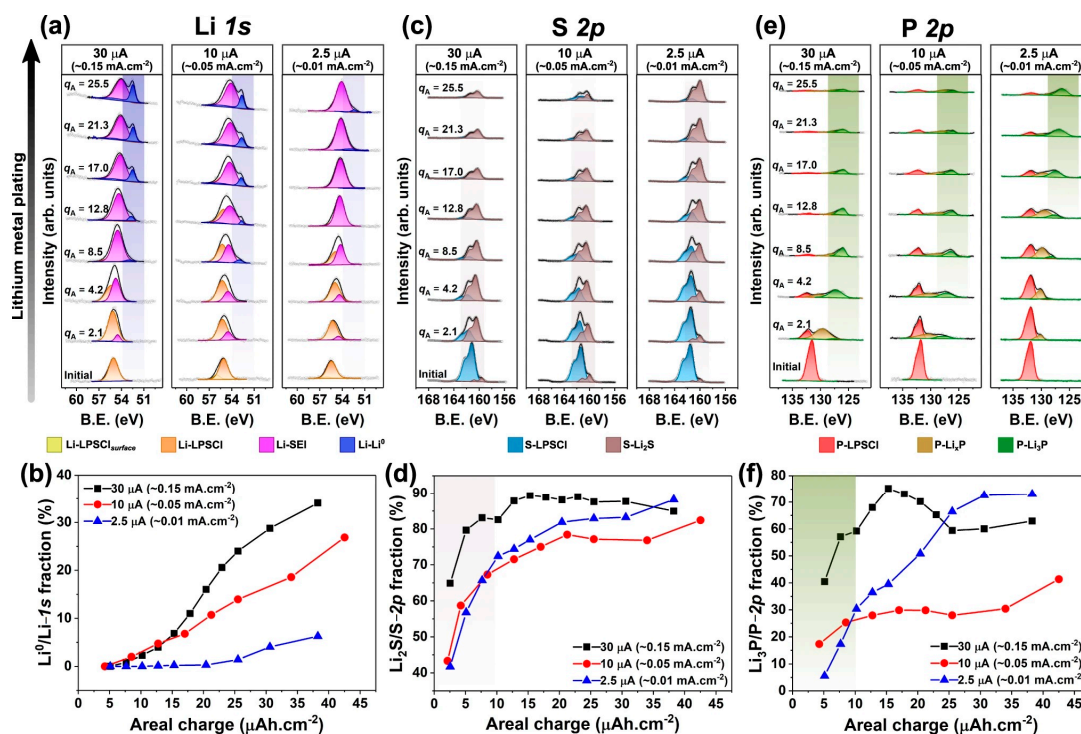


Figure 15. Evolution of X-ray photoemission spectroscopy (XPS) spectra during virtual electrode plating on an LPSCl surface at different electron beam currents (EBCs): 30 μA ($\sim 0.15 \text{ mA cm}^{-2}$, left), 10 μA ($\sim 0.05 \text{ mA cm}^{-2}$, center), and 2.5 μA ($\sim 0.01 \text{ mA cm}^{-2}$, right). The panel (a) Li-1s, panel (c) S-2p, and panel (e) P-2p transitions are shown for varying charge passed (q_A , $\mu\text{Ah cm}^{-2}$). Quantification reveals higher fractions of metallic Li (Li_0 , panel (b)), Li_2S (panel (d)) and Li_3P (green area in panel (f)) at high current densities, indicating accelerated interface kinetics and rapid formation of a metallic Li layer during plating [66].

In another work, Shadike et al. [67] studied the solid electrolyte interphase (SEI) composition in lithium metal anodes for high-energy batteries using synchrotron-based XRD and pair distribution function (PDF) analysis. The research addresses the debate on the presence of LiH in the SEI, offering evidence of its abundance and discussing the possibility of misidentification as LiF. Figure 16a shows XRD patterns of SEI samples cycled with low and high concentrations of lithium bis(fluorosulfonyl)imide (LiFSI) salt in different solvents. Figure 16b presents Rietveld refinement results, revealing the coexistence of crystalline phases such as lithium metal, Li_2O , and LiH in the SEI. Additionally, a distinct amorphous component, denoted as SEI-LiF, is identified with unique structural features. The research provides insights into SEI stability and sheds light on the role of LiH and LiF in lithium metal cells, enhancing the understanding of battery performance.

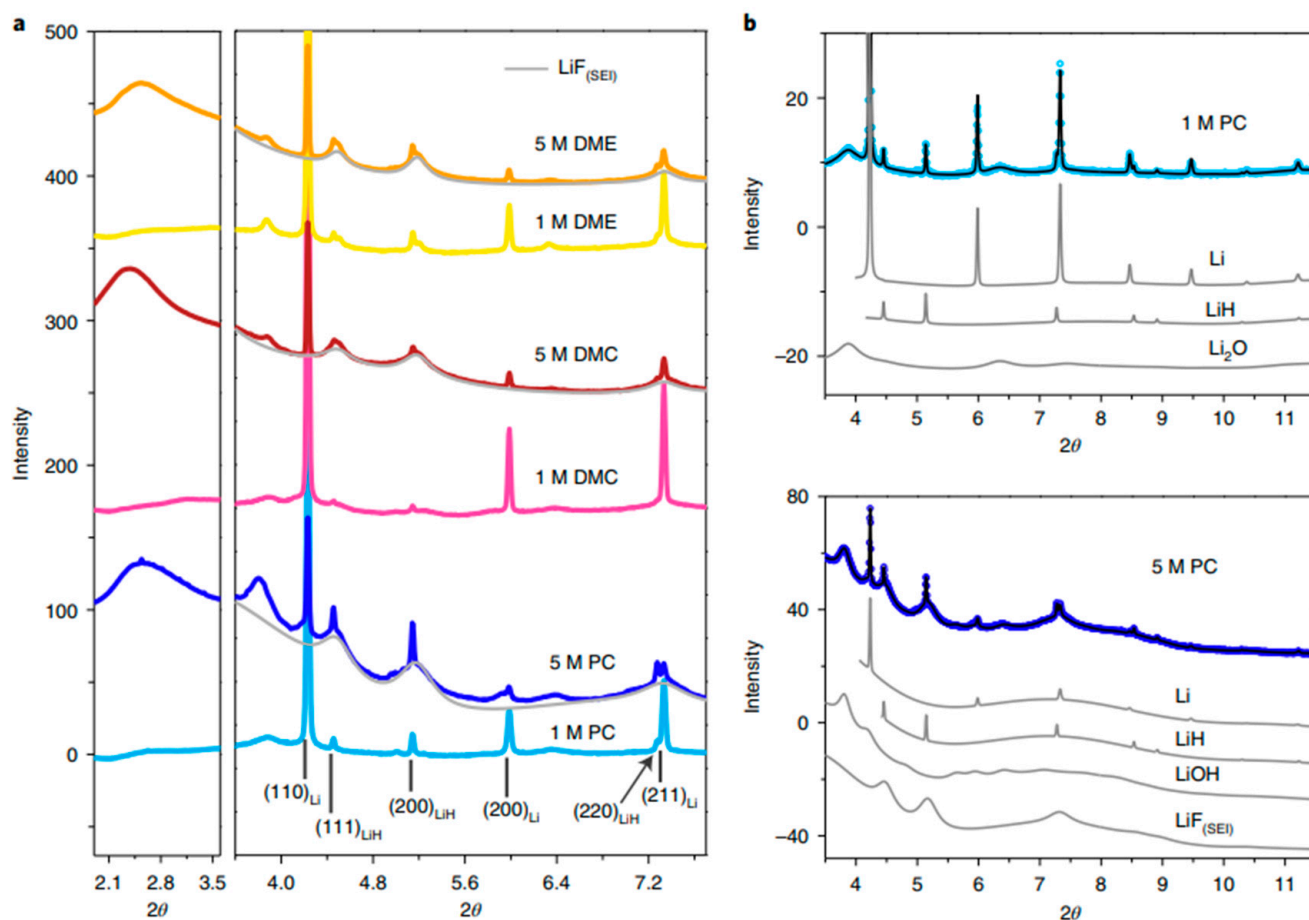


Figure 16. (a) Depiction of the XRD characterization of a solid electrolyte interphase (SEI) in lithium metal anodes utilizing LiFSI salt with varying concentrations (LCEs and HCEs) and solvents (PC, DMC, and DME). The light gray pattern corresponds to LiF (SEI), while the wavelength used is 0.18323 Å. (b) Rietveld refinement of SEI XRD data for low and high LiFSI concentrations in PC is presented. The contributions of individual phases to the XRD pattern are illustrated, with open circles representing experimental data and black lines representing calculated data [67].

2.2. Lithium Dendrite Growth

Dendrite formation in solid-state electrolytes, which is crucial for high-performance batteries, is linked to the shear modulus. Stacking pressure plays a vital role in influencing crack propagation, interface stability, and dendrite growth in these electrolytes [68]. For example, dendrite propagation across lithium lanthanum zirconate (LLZO) in solid-state electrolytes is attributed to metallic material formation at the Li-LLZO interface and grain boundaries, allowing for electron conduction and subsequent lithium deposition. This phenomenon, coupled with poor electrochemical stability leading to Li dendrite formation and O_2 generation, hinders high-performance batteries and compromises safety [68].

For lithium anodes to be a viable technology, significant challenges, especially regarding safety and cyclability, must be addressed. The deposition of lithium in dendritic form poses a major risk in regard to thermal runaway and explosions due to internal cell shorting. It is essential to achieve a dendrite-free lithium deposition given the diverse morphologies of dendrites [69], including needle-like [70], mossy-like [71], or fractal-like [72], which can grow under different conditions, as illustrated in Figure 17 [73].

Yu et al. [74] employed synchrotron-based X-ray imaging (XRI) to elucidate Li plating/stripping under operando and practical battery conditions, exploring the intricate influence of critical parameters on resulting Li metal morphology for the first time. Their systematic study addresses the crucial need for understanding lithium electrodeposition,

observing dendritic growth dynamics and establishing how morphology is influenced by various factors, including separator, ionic concentration, current density, electrolytes, and additives. The study utilizes a “V-slot holder” design (Figure 18) for precise control of areal current density during lithium (Li) plating. Figure 18c–e presents the effects of critical parameters, including the separator (which is crucial for minimizing distance, preventing short circuits in batteries), on Li plating/stripping. Li plating studies often neglect separator effects due to challenges in observing and quantifying Li plating under it. The separator, a vital battery component, significantly influences Li morphology, with denser Li layers forming near the separator during cycling, stressing the separator and potentially leading to battery short-circuiting (~ 7.5 h) [74].

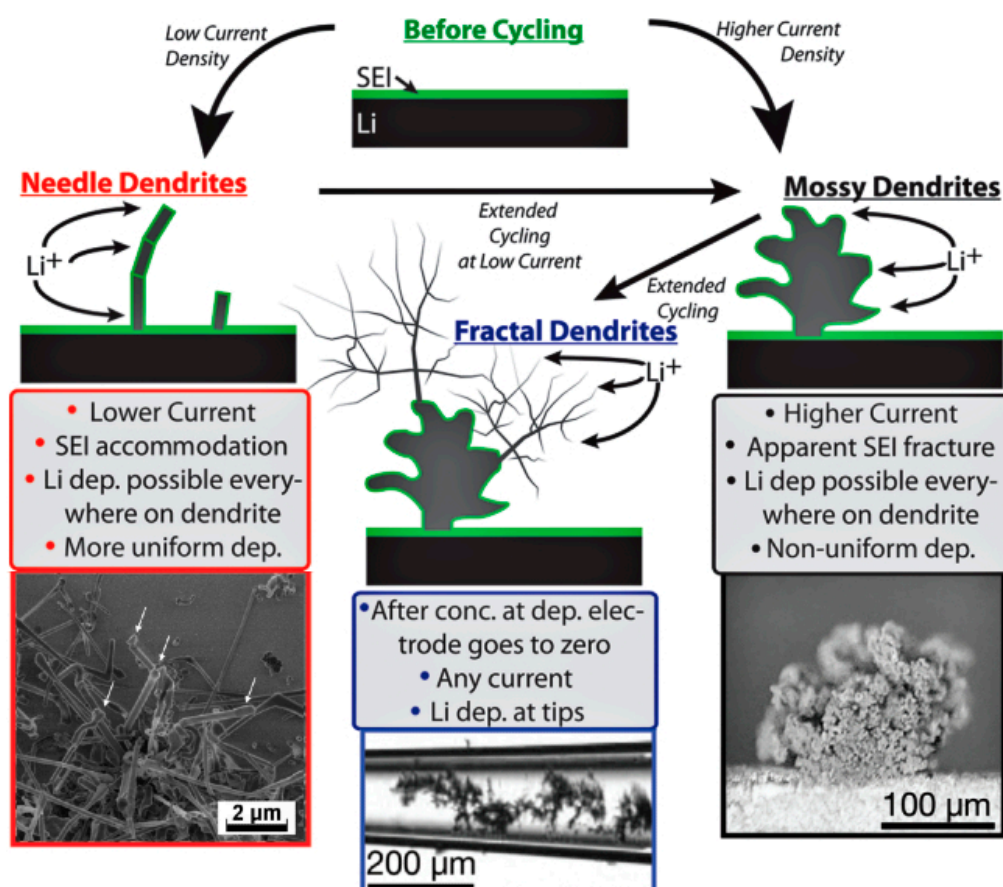


Figure 17. Illustration depicting various dendrite shapes presented alongside sample micrographs. Arrows highlight the possible shifts in morphological changes that can take place throughout cycling [73].

Most studies on dendrite growth in lithium batteries concentrated on Li deposition at the Li–SE interface (interface between the lithium metal and the SE), neglecting the subsurface dendrite structure. Harry et al. [75] utilized synchrotron X-ray microtomography to examine early dendrite development at the Li–polymer interface. Figure 19 illustrates the early stage, showcasing the bulk of dendrite beneath the interface before protrusion into the polymer electrolyte. The three-dimensional reconstructions vividly show that, in the early stages, most dendrites were buried under the electrode, significantly impacting dendrite nucleation compared to growth at the tip and side in the polymer electrolyte [76].

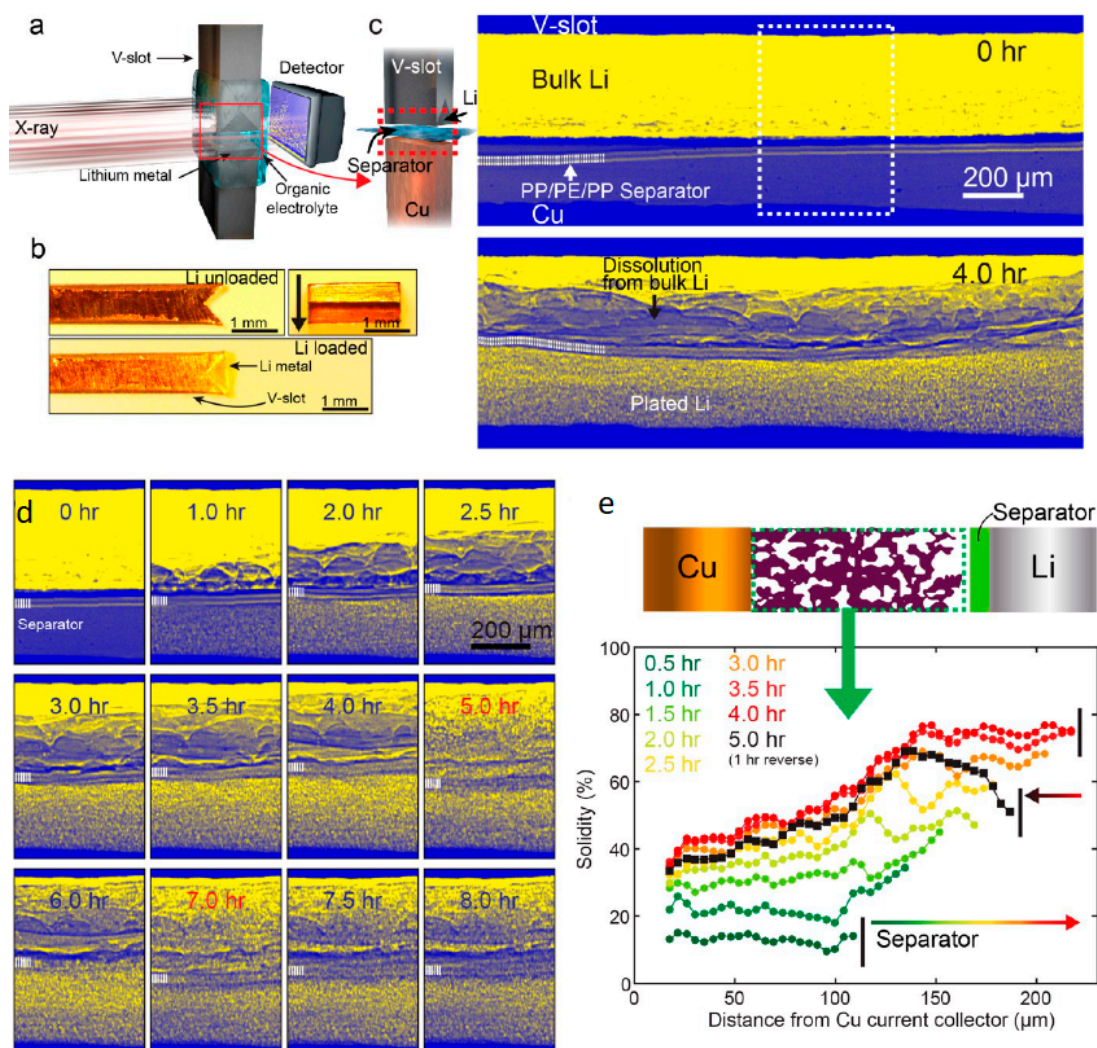


Figure 18. (a) Experimental arrangement for operando X-ray imaging using a V-slot Li electrode holder. (b) Optical microscopy of the V-slot holder before Li loading, showcasing side (top left) and top (top right) perspectives, and, after Li loading, featuring a side view (bottom). (c) Li plating/stripping behavior with a separator at 10.0 mA/cm^2 in $1.0 \text{ M LiPF}_6\text{-EC/DEC}$ before (right, top) and after 4 h plating (right, bottom), along with the experimental schematic (left). (d) Progression of Li plating/stripping cycles in a specified area (white dotted rectangle in (c)). (e) Solidity of plated Li beneath the separator relative to the distance from the Cu current collector [74].

Chen et al. [77] utilized X-ray photoelectron spectroscopy (XPS) to analyze the lithium metal negative electrode on a Cu-Zn alloy mesh collector, assessing the impact of heat treatments at $300 \text{ }^\circ\text{C}$ and $400 \text{ }^\circ\text{C}$. Results indicate that, at $400 \text{ }^\circ\text{C}$, the electrode displays reduced decomposition products, signifying diminished side reactions and improved stability (see Figure 20). XPS patterns highlight the presence of organic electrolyte by-products and LiTFSI (lithium salt in electrolyte) functional groups. Notably, the $400 \text{ }^\circ\text{C}$ -treated mesh exhibits an increased LiF content, which is recognized for enhancing the stability of the interfacial SEI film and preventing lithium dendrite formation. This finding emphasizes the heightened stability of the $400 \text{ }^\circ\text{C}$ -treated electrode interface, a critical factor in advancing battery performance.

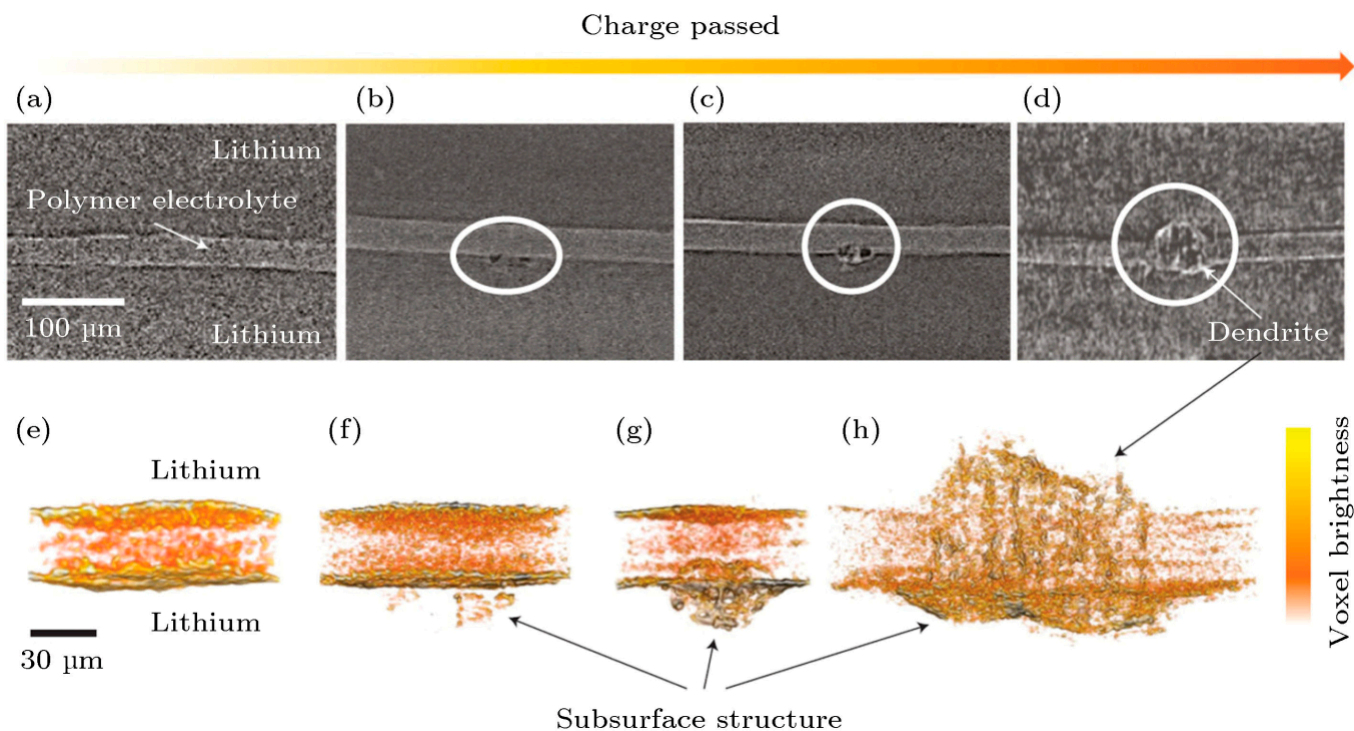


Figure 19. Progression of dendrite growth triggered by subsurface structure and redistributed charges at the Li–SE interface. XRT slides display cross-sections of a symmetric cell at different cycling points with varying amounts of charge passed: 0 C cm^{-2} (a), 9 C cm^{-2} (b), 84 C cm^{-2} (c), and a short cell at 296 C cm^{-2} (d). Additionally, magnified 3D reconstructed volumes of cells corresponding to an uncycled state ($C = 0 \text{ C cm}^{-2}$) (e), early cycling stage ($C = 9 \text{ C cm}^{-2}$) (f), intermediate cycling stage ($C = 84 \text{ C cm}^{-2}$) (g), and a shorted cell ($C = 296 \text{ C cm}^{-2}$) (h) are depicted [75].

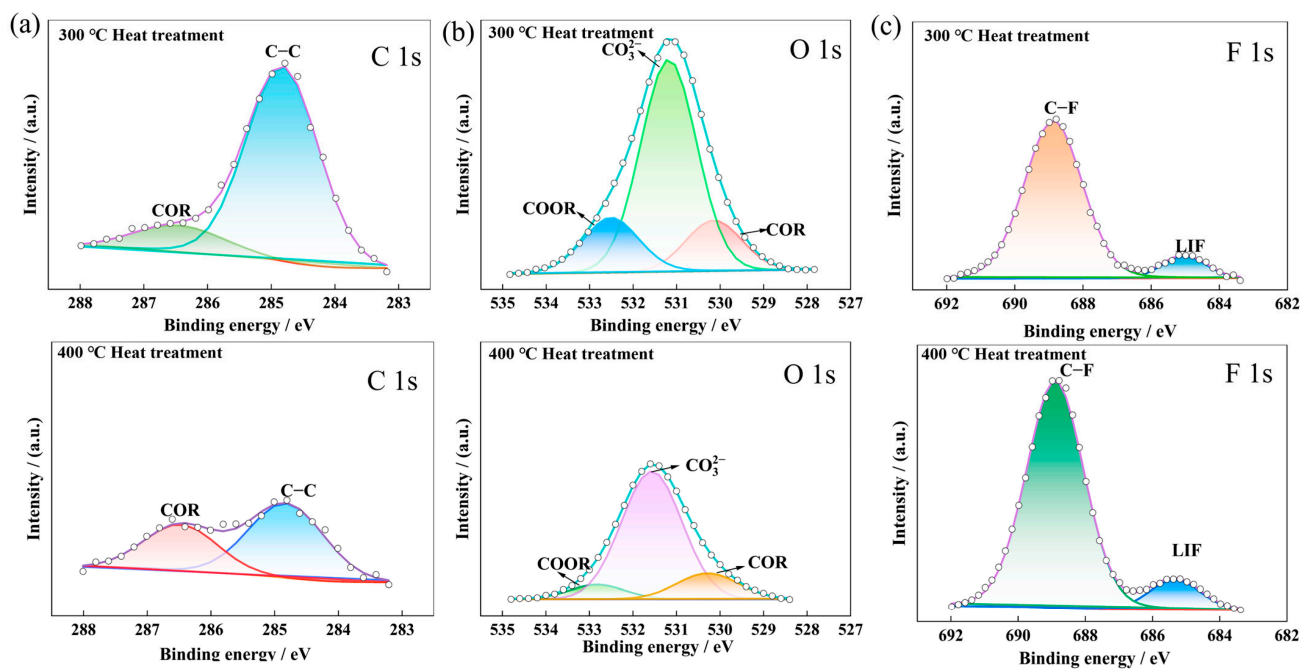


Figure 20. Analysis of X-ray photoelectron spectroscopy (XPS) patterns on the surface of the lithium metal negative electrode of the half-cell using a Cu–Zn alloy mesh electrode subjected to heat treatment at both 300 and 400 °C. The patterns include (a) C 1s, (b) O 1s, and (c) F 1s [77].

2.3. Chemical and Structural Changes in Electrode Materials

Lou et al. [78] investigate interfacial issues in solid-state batteries, emphasizing the impact of microstructural complexity and chemical heterogeneity on local interfacial chemistry. Figure 21a reveals a positive shift of 0.4 eV at the K-edge in cycled ASSLBs, indicating a significant increase in nickel valence, while Figure 21b shows a slight change in Ni-O and Ni-M peaks in cycled ASSLBs. The XANES and EXAFS analyses suggest heterogeneous SOC distribution in ASSLBs triggered by disconnected ion channels from cracks. Figure 21c demonstrates a significant negative shift in XRD analysis (0.04°) of cycled electrodes, indicating increased interplanar layer distance. Figure 21e exhibits a positive shift in the XANES absorption edge of the core region in ASSLBs, indicating heterogeneous SOC distribution triggered by disconnected ion channels from cracks (Regions 1 and 2 are determined in Figure 21d). These findings underscore the role of solid–solid interfaces and phase transformations, providing critical insights into interfacial transport mechanisms in solid-state batteries.

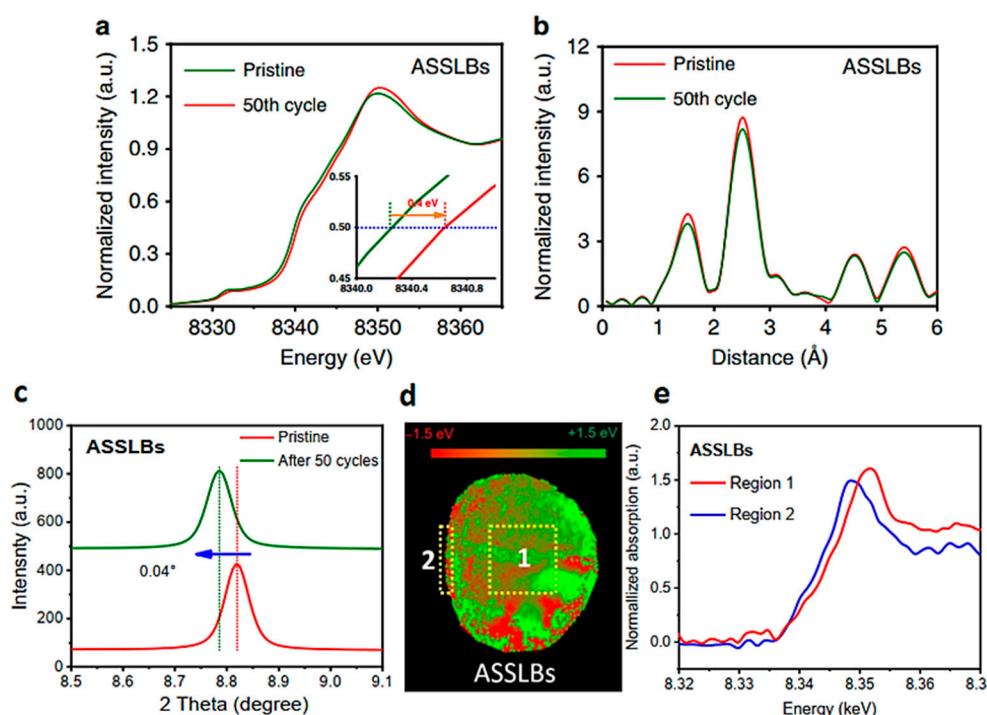


Figure 21. Structure and chemistry evolution of NCM particles during cycles in ASSLBs. (a,b) XANES and EXAFS analyses are performed on both the initial and 50-cycled electrodes. (c) XRD patterns shift prior to and after cycles. (d) Two-dimensional TXM-XANES mapping reveals cycled NCM particle characteristics. (e) The average XANES spectra of the core and interface regions in cracked particles within ASSLBs [78].

A novel electrochemical cell with Kapton X-ray windows was developed for in situ XAS at the Indus-2 Synchrotron Source in India. Testing involved LIBs with LiMn_2O_4 cathodes, revealing non-reversible electronic and structural changes during charging/discharging. This facility enables crucial investigations into cyclic instability in new-generation batteries [79]. The electrochemical cell for in situ XAS measurements was designed with a stainless-steel body, utilizing a cylindrical cavity to hold the battery stack. Figure 22a,b illustrate the detailed schematic design, featuring stainless steel disks, nylon sleeves, and airtight seals. X-ray transparent Kapton windows ensure proper transmission while maintaining hermeticity. Key components include a LiMn_2O_4 cathode, Li anode, and electrolyte with galvanostatic charge/discharge cycles conducted for performance evaluation [79].

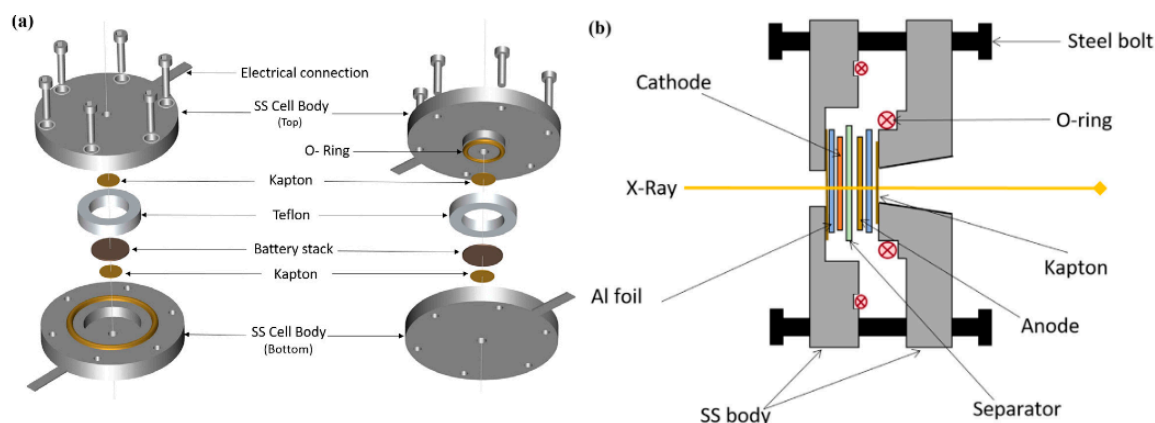


Figure 22. (a) A detailed schematic illustration of the internally developed in situ electrochemical (EC) cell in an exploded view. (b) Diagram outlining the configuration of the assembled in situ cell [79].

In Figure 23a,b, $\chi(R)$ versus R plots obtained from in situ XAS at Mn K-edge during charging and discharging cycles of $\text{Li}_{1-x}\text{Mn}_2\text{O}_4$ are presented. The plots reveal changes in local structure around Mn ions. Fitting plots provide insight into structural parameters during electrochemical processes. The Debye–Waller factors (σ^2) for Mn–O shells decrease during charging and increase during discharging, indicating a shift from two mixed Mn–O octahedra to a single Mn–O octahedra for charging state (Figure 24). Mn–Mn peak heights in higher order shells increase during charging and decrease during discharging, suggesting changes in Mn–O octahedral regularity. This in situ study highlights the non-reversible structural transformations in LiMn_2O_4 during electrochemical cycling [79].

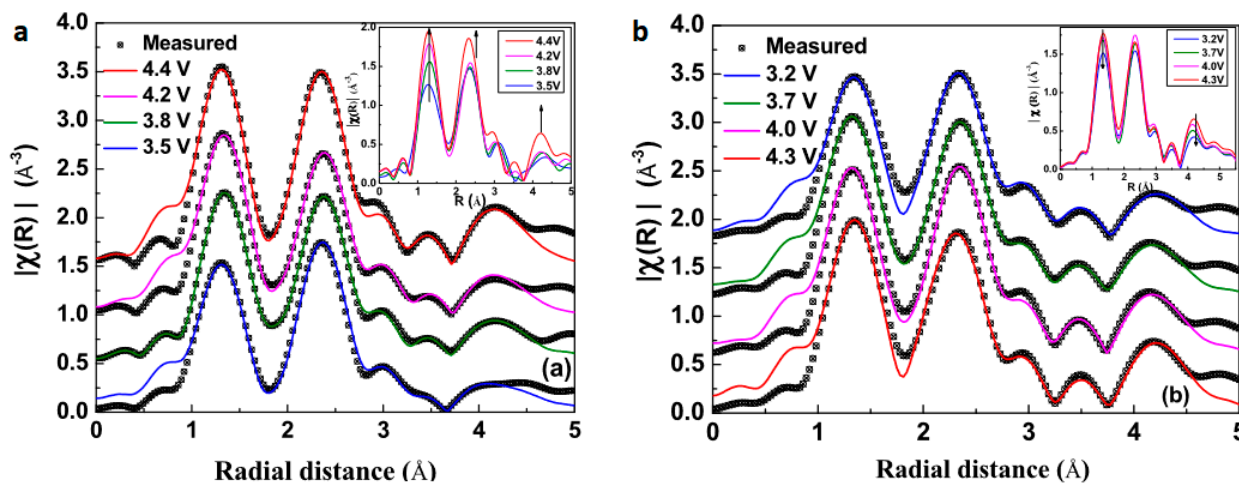


Figure 23. Experimental $\chi(R)$ versus R results for $\text{Li}_{1-x}\text{Mn}_2\text{O}_4$ samples recorded during (a) charging and (b) discharging at the Mn K-edge. The empty circles represent the measured data, and the full lines depict the best-fit theoretical plots. To enhance clarity, the plots are vertically shifted by 0.5 \AA^{-3} . The inset displays the plots in the same scale for a detailed examination. The initial peak at approximately 1.4 \AA indicates the presence of the nearest neighbor oxygen (O) shells, while the subsequent peak at around 2.4 \AA signifies the next nearest neighbor manganese (Mn) shells that surround the Mn atom undergoing absorption [79].

X-ray emission spectroscopy (XES) is explored as a promising alternative to synchrotron-based XAS for studying local electronic structures in materials. Addressing challenges posed by the intricate sulfur reduction mechanism during discharge highlights sulfur XES as a laboratory tool, providing insights into electrochemical processes in Li–S batteries. By showcasing the potential of sulfur XES as a laboratory tool, the research offers insights

into electrochemical processes in Li–S batteries, presenting a viable, accessible option for routine analysis in battery system studies. Kavčič et al. [80] explored X-ray emission spectroscopy (XES) as a laboratory analytical tool to characterize electrochemical processes within lithium–sulfur (Li–S) batteries. Figure 25a presents measured sulfur $K\alpha$ spectra of S_8 and Li_2S standards, representing the initial and final states during Li–S battery discharge. The energy shift between these spectra reflects the difference in electronic charge states. Figure 25b shows a correlation between measured energy shifts and theoretical sulfur average charge, demonstrating the capability of XES to determine the average charge (oxidation state) of sulfur within the Li–S battery cathode. This approach offers valuable insights for in-depth electrochemical analysis and could facilitate routine laboratory testing of Li–S batteries.

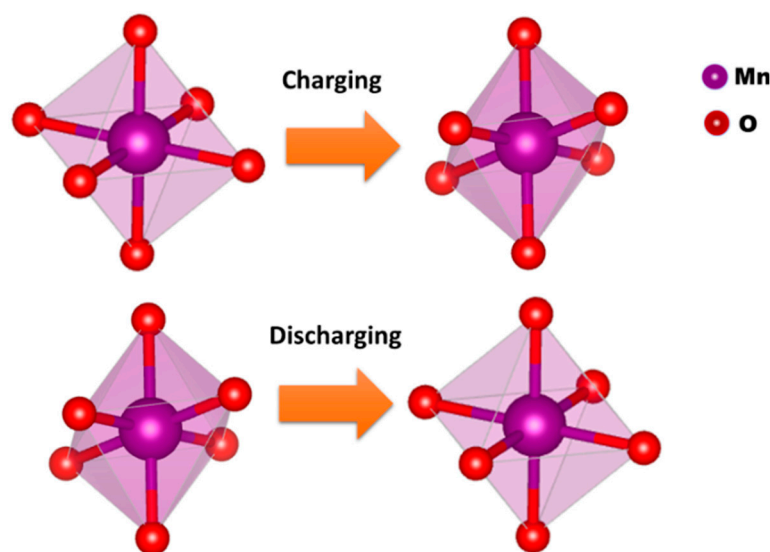


Figure 24. Schematic illustrating the crystal structures prior to charging and following discharging [79].

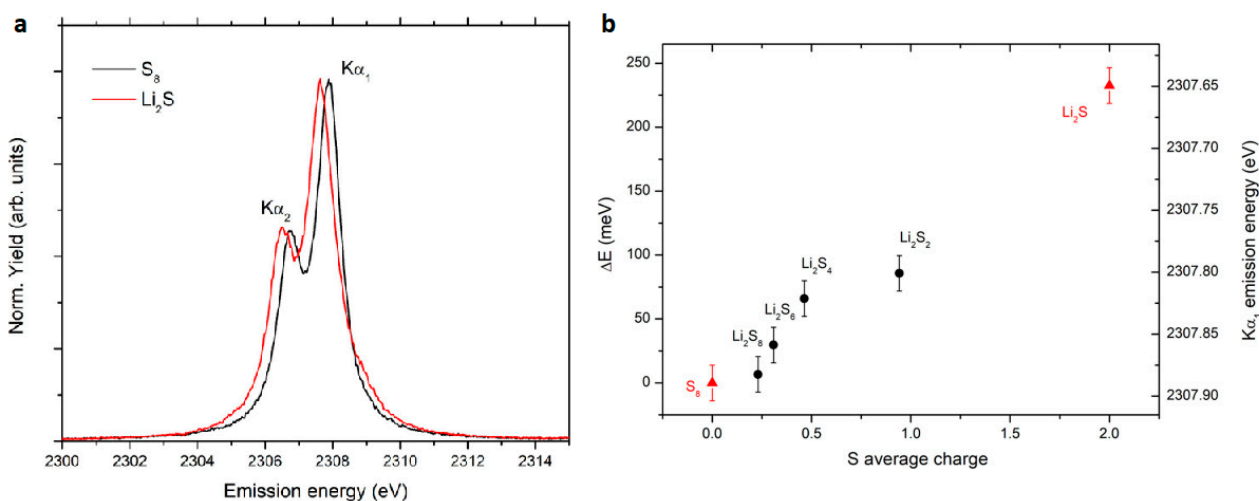


Figure 25. (a) High-energy resolution proton-induced $K\alpha_{1,2}$ sulfur X-ray emission spectra of Li_2S and α - S_8 standards. (b) Experimental $K\alpha_1$ absolute emission energies and energy shifts relative to the $K\alpha_1$ energy of elemental sulfur as a function of the theoretical average sulfur charge [80].

Rahe et al. [81] revealed the cathode electrode's structural changes through a CT cross-section, including the current collector and active material coating. The images of Figure 26, chosen from the sample center to avoid preparation influence, display the new and aged electrode for dimensional and structural comparison. An additional layer in the aged electrode, distinct from the active material and current collector, exhibits cracking and pinholes. This layer, potentially due to aluminum current collector corrosion, contributes to an expanded electrode thickness, varying from 158 μm to 174 μm . Notably, the layer thickness reaches up to 49 μm , indicating a substantial influence on electrode morphology and potential implications for cell performance.

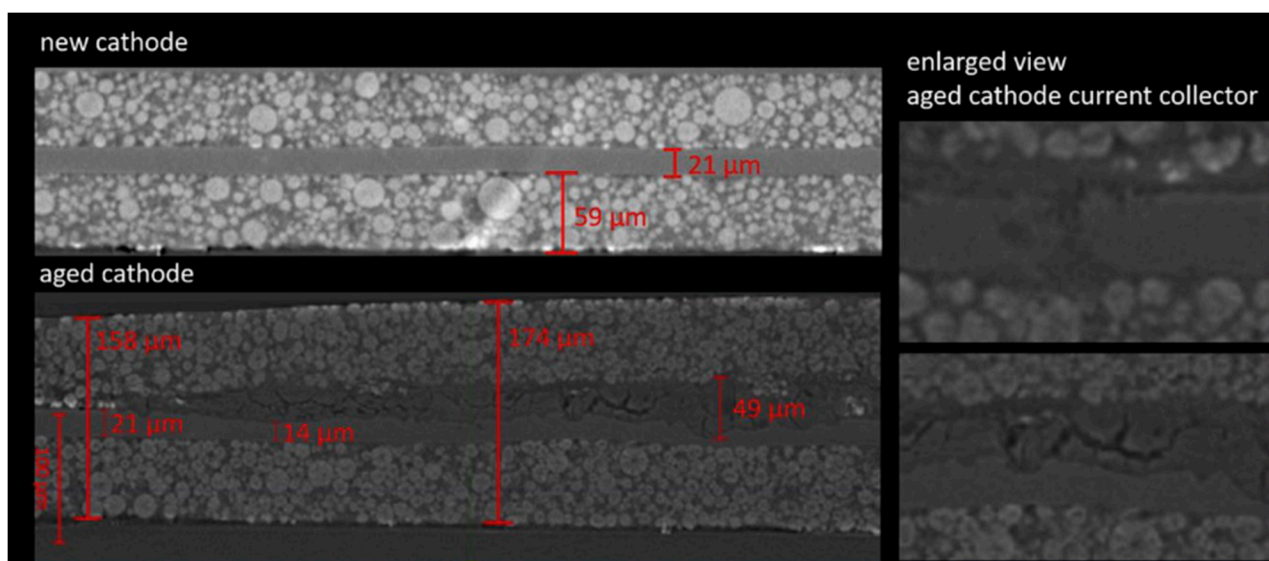


Figure 26. The aged cathode in an X-ray CT image captured using the ZEISS Xradia Versa. The image reveals the presence of cracked particles and an oxidized current collector [81].

Yao et al. [82] investigate LIB cycling dynamics using energy dispersive X-ray diffraction (EDXRD) with a setup at Argonne's Advanced Photon Source. Figure 27f depicts a transverse cross-section of the cell, revealing the graphite electrode, separator, cathode, and current collectors. The X-ray beams, penetrating from the left, form overlapping layers (L_0 to L_4) probing different sections of the cell during lithiation and delithiation. The colored lines represent the X-ray beam profiles. The study aims to understand lithium gradients and heterogeneities in the porous graphite electrode during cycling, which is crucial for optimizing battery performance. In Figure 27a–e, XRD patterns from the cycle of Gr/NCM523 cell cycling are highlighted. The patterns reveal major features of Li_xC_6 phases during lithiation and delithiation. Figure 27g displays corresponding d-spacings for these phases, with Stages I (LiC_6), II (LiC_{12}), and III (LiC_{18}) being represented by specific peaks. The XRD patterns elucidate distinctive steps in the slow C/20 cycle, attributed to graphite electrode stages, while at a faster 1C rate, these steps blur due to lithium heterogeneity. A well-separated LiC_6 phase peak at 3.7 \AA is observed, originating in the final stages of lithiation. The study highlights dynamic changes in phase concentrations across layers during lithiation and delithiation, providing insights into electrode behavior.

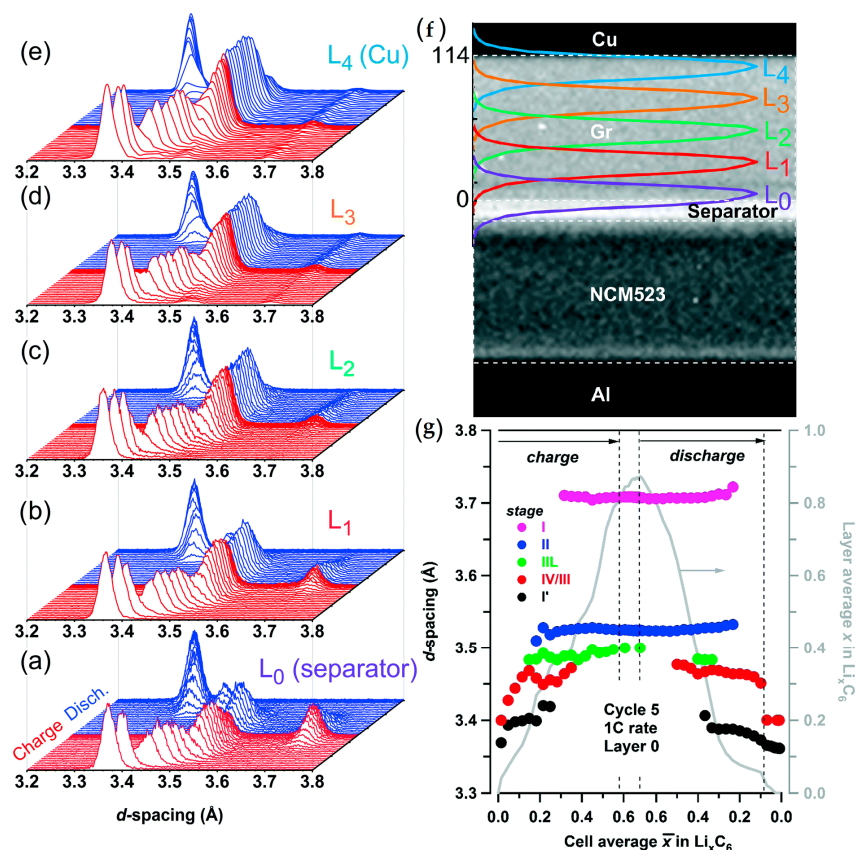


Figure 27. XRD patterns within the 3.2–3.8 Å d-spacing range obtained during 1C charge and discharge cycles. Panels (a–e) correspond to layers L_0 to L_4 , respectively, labeled in (f). Normalized diffraction intensities are presented on a consistent scale, with red indicating charge and blue indicating discharge. Different Bragg peaks signify distinct stages of graphite lithiation. (f) A transverse X-ray radiograph illustrates the cell’s cross-section, featuring components like the 10 μm Cu current collector, 114 μm porous graphite electrode, separator, 111 μm cathode, and 20 μm Al current collector. Gaussian-shaped lines depict the X-ray beam profiles. Probing overlapping layers (L_n) during charge and discharge showcase lithium-ion movement. Panel (g) exhibits experimental d-spacing for Li_xC_6 phases in layer L_0 during 1C cycling, plotted against the cell’s average lithium content (% x). Lithiation stages are color coded, and vertical dashed lines indicate potentiostatic holds. Layer average lithium content (x) is shown on the right [82].

2.4. Mechanical Degradation

Insufficient physical contact and uneven contact points can hinder lithium-ion transport and degrade rate performance at solid–solid interfaces [83]. Sun et al. [84] employed operando synchrotron X-ray nano tomography and in situ 3D XANES spectroscopy to investigate the microstructural evolution and phase distribution in FeS_2 particles within solid-state batteries. The distinctive attenuation coefficients in elements with varying depths of discharge (DOD) facilitate the differentiation of FeS_2 compositions, which have high X-ray absorption at the iron K-edge, from lighter elements like $\text{Li}_7\text{P}_3\text{S}_{11}$ electrolyte. Utilizing the TXM-XANES approach allows for obtaining not only morphology and element identification but also high-resolution chemical information by tuning hard X-ray energy across the Fe K-edge. In situ 3D XANES measurements were conducted to explore chemical homogeneity and phase distribution in real 3D within FeS_2 particles. Chemical maps were generated through linear combination fitting with XANES spectra of standard phases. The converted Fe phase front induces significant volume expansion and cracks in FeS_2 particles, with subsequent phase propagation slowing down and terminating at low discharging potentials. Quantitative analysis confirms the complex, heterogeneous nature of the phase

evolution, emphasizing challenges in solid–solid interfaces and potential contact losses during electrochemical reactions. Figure 28A depicts the phase distribution during discharging states, revealing a heterogeneous phase conversion of FeS_2 . In Figure 28B, discharged FeS_2 at DOD-3 shows a converted Fe phase front progressively penetrating the particle, leading to large volume expansion and cracks. The core–shell model at the final discharging state is suggested in Figure 28C, with associated XANES spectra (Figure 28D) and quantitative analysis (Figure 28E) indicating the termination of the conversion reaction at low potentials in solid-state batteries.

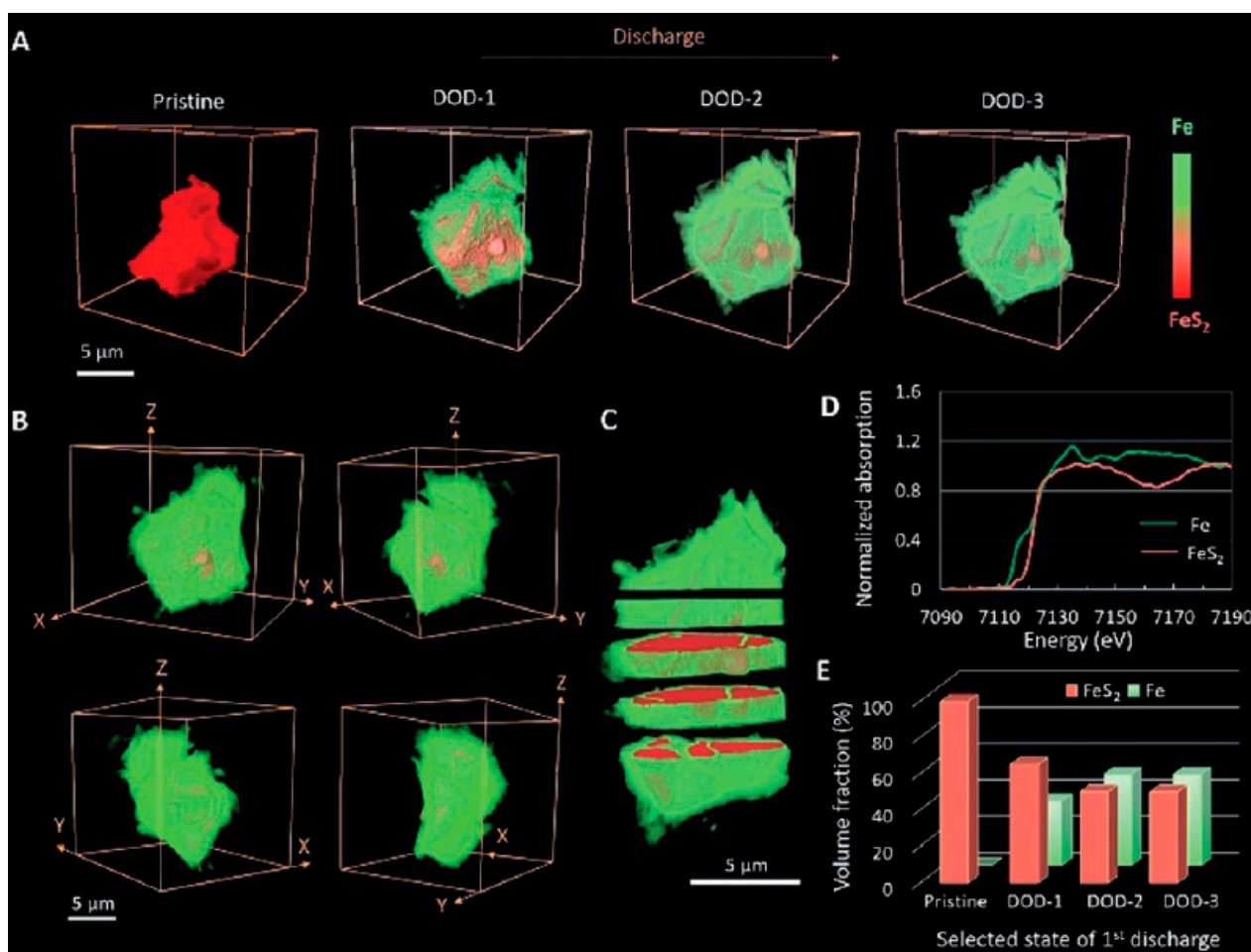


Figure 28. Operando X-ray spectroscopic nano tomography. (A) The evolution of phase distribution during discharging, (B) images of discharged FeS_2 at DOD-3 from various angles, (C) a cross-sectional view of lithiated FeS_2 , (D) XANES spectra comparing standard FeS_2 and Fe, and (E) the phase volume fraction derived from thorough 3D quantitative analysis [84].

In 2013, Ebner et al. [85] conducted the first operando tomographic experiment on lithium batteries, tracking SnO expansion to $\text{Li}_2\text{O} + \text{Li}_{4.4}\text{Sn}$. Core-shell lithiation behavior in SnO particles (Figure 29) was observed, proving consistent with antimony and tin particles. They found zigzag cracking in SnO particles, which were attributed to pre-existing defects in the (001) plane along the [010] crystallographic direction, as shown in Figure 29. This cracking is linked to volumetric changes during (de)lithiation, emphasizing the role of particle size and morphology [46].

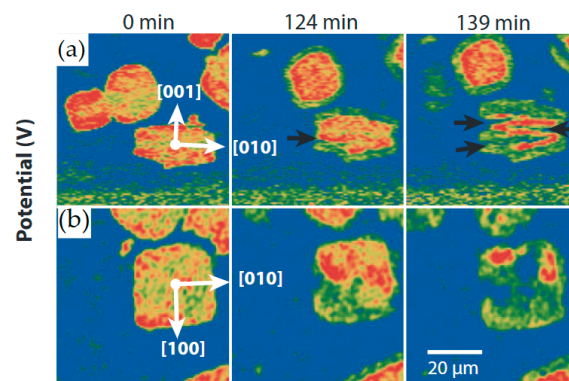


Figure 29. Tomographic data of SnO particles captured at various times of lithiation, presenting virtual cross-sections. Subpanels (a,b) display the particles along horizontal and vertical cuts, respectively. The white arrows denote crystallographic directions, while the black arrows signify locations of crack formation [46,85].

Ziesche et al. [86] employ high-throughput X-ray CT to investigate lithium intercalation and electrode degradation in a commercial CR2 Li-ion primary cell. The X-ray images reveal mechanical degradation, highlighting cracks in the cathode originating from the production process. During discharge, the cathode undergoes heterogeneous expansion, causing cracks to propagate. The X-ray CT detect mechanical degradation. The virtual ‘unrolling’ of 3D tomograms aids in data visualization and correlation, offering new insights into battery performance. Figure 30 displays high-speed X-ray tomograms at different states of charge, illustrating changes in cathode morphology and mechanical degradation during discharging. The study’s correlative imaging methodology sets a benchmark for battery characterization that is applicable to various geometries and chemistries.

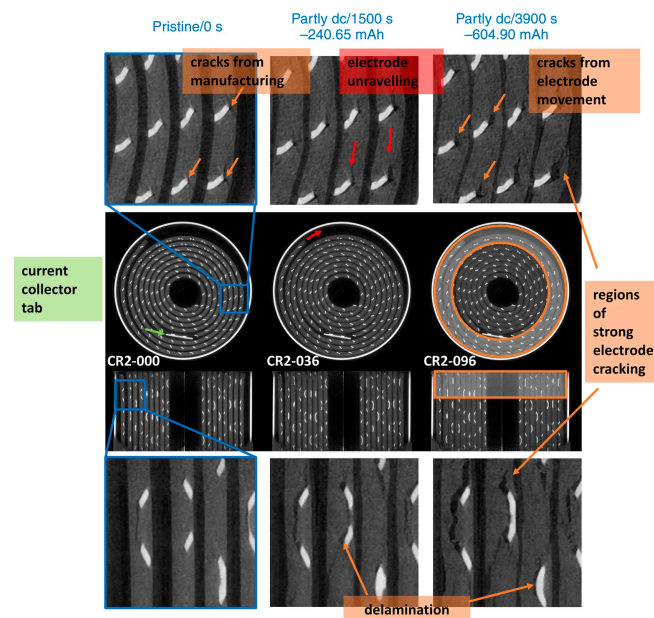


Figure 30. Cross-sectional views, both horizontally and vertically, extracted from X-ray tomograms. A total of 103 tomograms, labeled from CR2-000 to CR2-102, were captured, with each tomogram recorded every 40 s over a 2.8-s acquisition period. The presented states include the pristine condition and two partially discharged states, showcasing the cracking and expansion of the MnO₂ electrode during cell discharge. The highly absorbent steel casing appears as a bright ring surrounding the wound membrane–electrode assembly. Contrast adjustments were made to enhance visibility of lower attenuating components [86].

2.5. Safety and Thermal Management

Pham et al. [87] investigate the prevention of thermal runaway in lithium-ion cells using metal-coated polymer current collectors (PCCs) compared to conventional metallic current collectors. Figure 31A,B illustrate the nail-penetration testing (a test in LIBs which simulates internal short circuit to assess safety against mechanical abuse, fire, and bursting [88]) of two cell types: G4-01, with standard commercial aluminum and copper current collectors, and G1-01, with aluminum PCC and a copper current collector, respectively. In G4-01, thermal runaway occurs immediately upon penetration, leading to electrode disintegration and widespread failure. Contrastingly, G1-01 exhibits a more ductile response, with the PCC preventing thermal runaway by shrinking away from the nail, maintaining electrode integrity. Operando synchrotron radiography captures the dynamic process, revealing the crucial role of the PCC in isolating the cathode and preventing thermal runaway. The PCC's ability to shrink and interrupt thermal breakdown, as evidenced by post-mortem-computed tomography, highlights its effectiveness in enhancing battery safety. These findings offer insights into the potential of metal-coated polymer current collectors for producing safer LIBs with improved performance and reduced manufacturing costs.

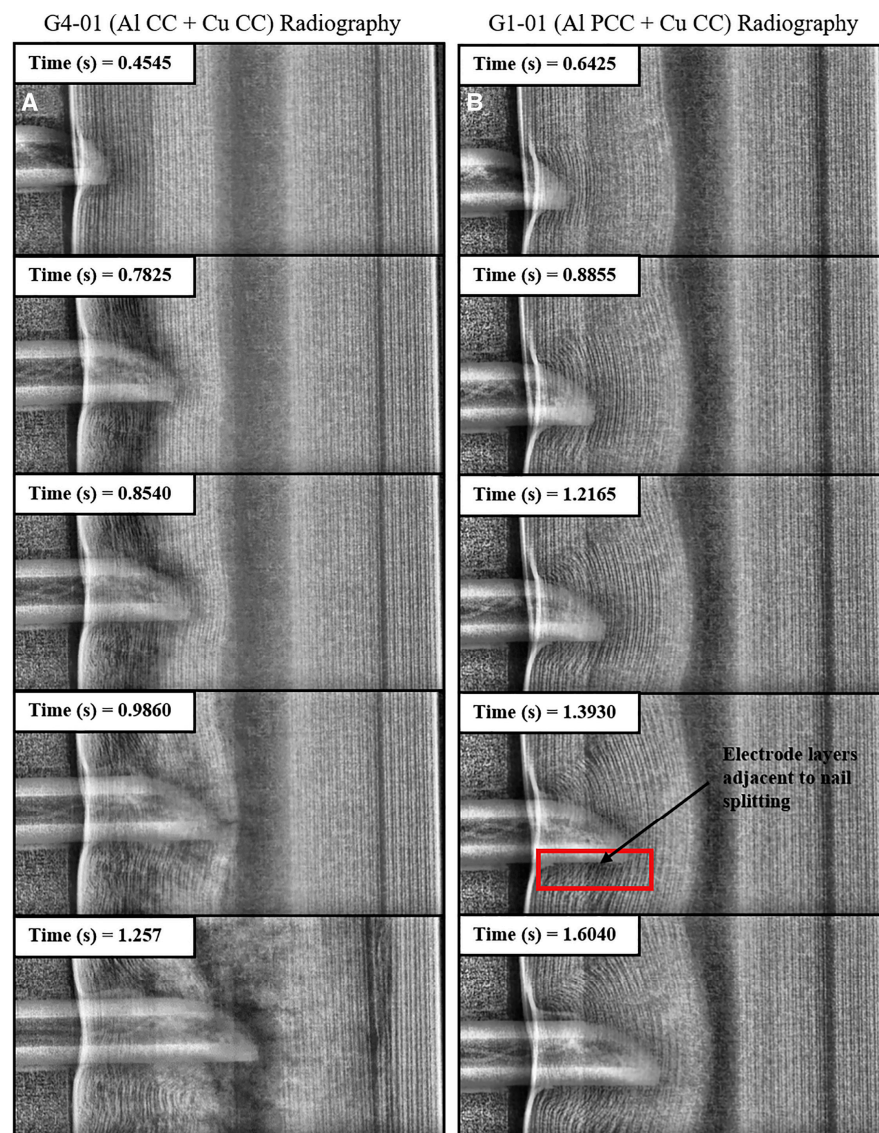


Figure 31. Imaging the cells during the process of nail penetration reveals that penetration persists until a depth of 9 mm or until further penetration by the nail is hindered. Each frame displays timestamps

in the top-left corner. (A) G4-01 (with standard commercial aluminum current collector and standard commercial copper current collector) experiences an immediate onset of thermal runaway upon penetration. The fourth frame illustrates evident cracking of the electrode assembly. (B) G1-01 (with aluminum-coated polymer current collector and standard commercial copper current collector) demonstrates a complete absence of thermal runaway, showcasing a distinct shear stress applied to the cylindrical electrode assembly [87].

Patel et al. [2] explores thermal failure and its impact on electrode materials in a commercial battery by employing multi-length scale X-ray CT. The study uses macroscale X-ray CT to examine architectural changes in a fully charged lithium-ion cell before and after failure (Figure 32). Figure 32a presents a 3D reconstruction of the cell prior to failure with orthogonal slices, while Figure 32b illustrates post-failure changes, including gas propagation from SEI layer decomposition and delamination (arrow 1) of the cathode material. Arrows 2 and 3 indicate alterations to the outer casing and electrode layers of the cell, with increased internal pressure causing expansion of the ridge marked by Arrow 2 and observable changes in the arrangement of the electrode layers. The non-destructive nature of X-ray CT allows visualization of internal cell structure collapse and the role of a cylindrical mandrel during thermal runaway.

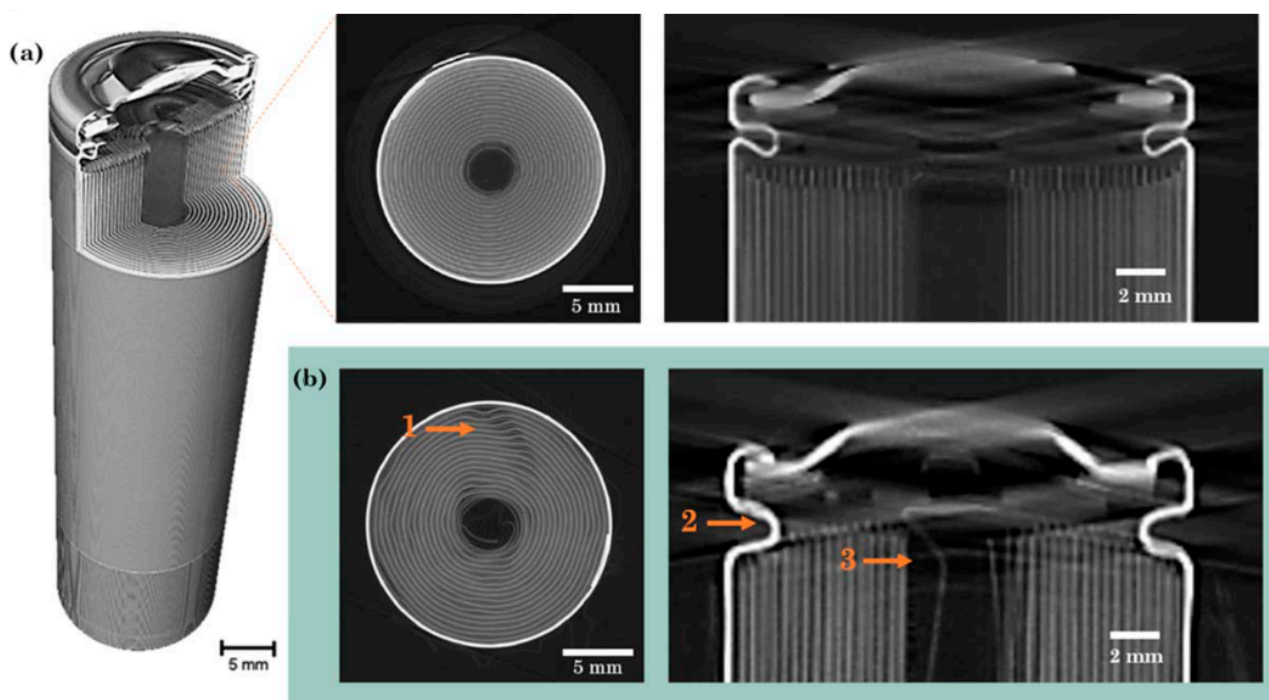


Figure 32. X-ray macro-CT findings of a commercial 18650 cell illustrate (a) a 3D reconstruction of the entire cell and cross-sectional views in the XY and YZ planes prior to thermal runaway and (b) cross-sectional views in the XY and YZ planes after thermal runaway, highlighting regions of deformation in the cell structure indicated by arrows [2].

3. Conclusions

In this review, we have studied various degradation mechanisms in LIBs through the lens of X-ray spectroscopies, as summarized in Table 1. These techniques, including XRD, XRT, TXM, XPS, and XAS (EXAFS and XANES), have been instrumental in uncovering critical phenomena, such as structural transformations, delamination, electrode morphology, chemical changes, crack detection, and more.

Table 1. Identified and tracked phenomena of LIBs by X-ray in situ techniques.

	Phenomena	XRD	XRT	TXM	XPS	XAS (EXAFS)	XAS (XANES)
Structural Analysis and Morphology	Tracking phase transformations	[82]	[84]	-	-	[78]	[78]
	Delamination, pulverization, and structural separation	-	[2]	-	-	-	-
	Electrode morphology	-	[81,86]	[84]	-	-	-
	Internal Structures in Bulk Materials	-	-	[61]	-	-	-
	Chemical and Structural Changes in Electrode Materials	-	[81]	-	-	[79]	-
	Crack Detection	-	[81,85,86]	-	-	-	-
	3D material distribution in All-Solid-State Batteries	-	[52]	-	-	-	-
	Dual-phase solid solution behavior	[54,67]	-	-	-	-	-
	Studying LIBs at various scales (cell level, electrode microstructures)	-	[2]	-	-	-	-
Thermal Behavior and Safety	Thermal runaway/Thermal failure	-	[2,87]	-	-	-	-
Chemical Characterization	Effective Charge	-	-	-	-	-	[55,78]
	Element Identification	-	-	-	-	-	[84]
	Chemical Bonding Type Determination	-	-	-	[60]	[78]	-
	Coordination Number Determination	-	-	-	-	[55]	-
	Chemical Bonding Length	-	-	-	-	[79]	-
	Lithium Intercalation and Electrode Degradation	-	[86]	-	-	-	-
	SEI Composition in Lithium Metal Anodes	[67]	-	-	[66]	-	-
	Lithium Metal Electrodeposition	-	-	[62]	-	-	-
Interface and Dendrite Dynamics	SEI Layer Formation	-	-	-	[58,77]	-	-
	Evolution of SEI at Li Metal Electrode Interface	-	-	-	[66]	-	-
	Lithium Dendrite Growth Dynamics	-	[75]	-	-	-	-
	Inhomogeneities during Delithiation/Lithiation	[82]	-	-	-	-	-

Despite the valuable insights gained, it is evident that dynamic observations of LIBs are crucial for advancing our understanding of their failure mechanisms and enhancing structural integrity. X-ray imaging, with its impressive temporal and spatial resolution, provides a powerful tool; however, challenges persist, particularly in its limited sensitivity to light Li and specifically in materials with high atomic numbers commonly found in current collectors (Al and Cu) or active materials (Co, Fe, Mn, and Ni) [89].

To address these challenges, there is a pressing need for more accurate spectroscopy techniques. Improving our ability to dynamically observe LIBs will not only provide

deeper insights into their intricate behaviors but will also pave the way for mitigating failures and optimizing battery structures. This review underscores the importance of ongoing research efforts in refining X-ray methodologies to meet the evolving demands of lithium-ion battery studies.

Funding: This research received no external funding.

Conflicts of Interest: The authors declare no conflicts of interest.

References

1. Detka, K.; Górecki, K. Selected Technologies of Electrochemical Energy Storage—A Review. *Energies* **2023**, *16*, 5034. [[CrossRef](#)]
2. Patel, D.; Robinson, J.B.; Ball, S.; Brett, D.J.L.; Shearing, P.R. Thermal Runaway of a Li-Ion Battery Studied by Combined ARC and Multi-Length Scale X-ray CT. *J. Electrochem. Soc.* **2020**, *167*, 090511. [[CrossRef](#)]
3. Sharova, V. Enhancing the Performance of Lithium Batteries through the Development of Improved Electrolyte Formulation, Formation Protocol and Graphite Surface Modification. Ph.D. Thesis, Karlsruher Institut für Technologie (KIT), Karlsruhe, Germany, 2018.
4. Han, S. Structure and Dynamics in the Lithium Solvation Shell of Nonaqueous Electrolytes. *Sci. Rep.* **2019**, *9*, 5555. [[CrossRef](#)]
5. Lee, J.; Kim, Y.-J.; Jin, H.S.; Noh, H.; Kwack, H.; Chu, H.; Ye, F.; Lee, H.; Kim, H.-T. Tuning Two Interfaces with Fluoroethylene Carbonate Electrolytes for High-Performance Li/LCO Batteries. *ACS Omega* **2019**, *4*, 3220–3227. [[CrossRef](#)]
6. Chen, Z.; Qin, Y.; Dong, Z.; Zheng, J.; Liu, Y. Numerical Study on the Heat Generation and Thermal Control of Lithium-Ion Battery. *Appl. Therm. Eng.* **2023**, *221*, 119852. [[CrossRef](#)]
7. Ma, S.; Jiang, M.; Tao, P.; Song, C.; Wu, J.; Wang, J.; Deng, T.; Shang, W. Temperature Effect and Thermal Impact in Lithium-Ion Batteries: A Review. *Prog. Nat. Sci. Mater. Int.* **2018**, *28*, 653–666. [[CrossRef](#)]
8. Diaconu, B.; Cruceru, M.; Anghelescu, L.; Racoceanu, C.; Popescu, C.; Ionescu, M.; Tudorache, A. Latent Heat Storage Systems for Thermal Management of Electric Vehicle Batteries: Thermal Performance Enhancement and Modulation of the Phase Transition Process Dynamics: A Literature Review. *Energies* **2023**, *16*, 2745. [[CrossRef](#)]
9. Zhang, J.; Shao, D.; Jiang, L.; Zhang, G.; Wu, H.; Day, R.; Jiang, W. Advanced Thermal Management System Driven by Phase Change Materials for Power Lithium-Ion Batteries: A Review. *Renew. Sustain. Energy Rev.* **2022**, *159*, 112207. [[CrossRef](#)]
10. Müller, M.; Schneider, L.; Bohn, N.; Binder, J.R.; Bauer, W. Effect of Nanostructured and Open-Porous Particle Morphology on Electrode Processing and Electrochemical Performance of Li-Ion Batteries. *ACS Appl. Energy Mater.* **2021**, *4*, 1993–2003. [[CrossRef](#)]
11. Huang, X.; Li, Y.; Acharya, A.B.; Sui, X.; Meng, J.; Teodorescu, R.; Stroe, D.-I. A Review of Pulsed Current Technique for Lithium-Ion Batteries. *Energies* **2020**, *13*, 2458. [[CrossRef](#)]
12. Hou, P.; Chu, G.; Jian, G.; Zhang, Y.; Zhang, L. Li-Ion Batteries: Phase Transition. *Chin. Phys. B* **2015**, *25*, 016104. [[CrossRef](#)]
13. Finegan, D.P.; Scheel, M.; Robinson, J.B.; Tjaden, B.; Michiel, M.D.; Hinds, G.; Brett, D.J.L.; Shearing, P.R. Investigating Lithium-Ion Battery Materials during Overcharge-Induced Thermal Runaway: An Operando and Multi-Scale X-ray CT Study. *Phys. Chem. Chem. Phys.* **2016**, *18*, 30912–30919. [[CrossRef](#)]
14. Lou, S.; Sun, N.; Zhang, F.; Liu, Q.; Wang, J. Tracking Battery Dynamics by Operando Synchrotron X-ray Imaging: Operation from Liquid Electrolytes to Solid-State Electrolytes. *Acc. Mater. Res.* **2021**, *2*, 1177–1189. [[CrossRef](#)]
15. Wang, J.; Chen-Wiegart, Y.K.; Wang, J. In Operando Tracking Phase Transformation Evolution of Lithium Iron Phosphate with Hard X-ray Microscopy. *Nat. Commun.* **2014**, *5*, 4570. [[CrossRef](#)]
16. Adam, R.; Lepple, M.; Mayer, N.A.; Cupid, D.M.; Qian, Y.; Niehoff, P.; Schappacher, F.M.; Wadewitz, D.; Balachandran, G.; Bhaskar, A.; et al. Coexistence of Conversion and Intercalation Mechanisms in Lithium Ion Batteries: Consequences for Microstructure and Interaction between the Active Material and Electrolyte. *Int. J. Mater. Res.* **2017**, *108*, 971–983. [[CrossRef](#)]
17. Nitta, N.; Wu, F.; Lee, J.T.; Yushin, G. Li-Ion Battery Materials: Present and Future. *Mater. Today* **2015**, *18*, 252–264. [[CrossRef](#)]
18. Vijayan, B.L.; Yasin, A.; Misnon, I.I.; Karuppiah, C.; Yang, C.-C.; Jose, R. Lithium-Ion Adsorption on Surface Modified Porous Carbon. *J. Energy Storage* **2023**, *71*, 108221. [[CrossRef](#)]
19. Hagen, M.; Yan, J.; Cao, W.J.; Chen, X.J.; Shellikeri, A.; Du, T.; Read, J.A.; Jow, T.R.; Zheng, J.P. Hybrid Lithium-Ion Battery-Capacitor Energy Storage Device with Hybrid Composite Cathode Based on Activated Carbon / LiNi_{0.5}Co_{0.2}Mn_{0.3}O₂. *J. Power Sources* **2019**, *433*, 126689. [[CrossRef](#)]
20. Zhao, S.; Yan, K.; Zhang, J.; Sun, B.; Wang, G. Reaction Mechanisms of Layered Lithium-Rich Cathode Materials for High-Energy Lithium-Ion Batteries. *Angew. Chem. Int. Ed.* **2021**, *60*, 2208–2220. [[CrossRef](#)]
21. Anitha Sukkurji, P. Advanced Anode and Cathode Materials for Li-Ion Batteries: Application to Printing Methodology. Ph.D. Thesis, Karlsruher Institut für Technologie (KIT), Karlsruhe, Germany, 2021.
22. Baig, N. Two-Dimensional Nanomaterials: A Critical Review of Recent Progress, Properties, Applications, and Future Directions. *Compos. Part Appl. Sci. Manuf.* **2023**, *165*, 107362. [[CrossRef](#)]
23. Li, Q.; Chen, D.; Tan, H.; Zhang, X.; Rui, X.; Yu, Y. 3D Porous V₂O₅ Architectures for High-Rate Lithium Storage. *J. Energy Chem.* **2020**, *40*, 15–21. [[CrossRef](#)]

24. Paras, Yadav, K.; Kumar, P.; Teja, D.R.; Chakraborty, S.; Chakraborty, M.; Mohapatra, S.S.; Sahoo, A.; Chou, M.M.C.; Liang, C.-T.; et al. A Review on Low-Dimensional Nanomaterials: Nanofabrication, Characterization and Applications. *Nanomaterials* **2023**, *13*, 160. [[CrossRef](#)]
25. Zhu, P.; Slater, P.R.; Kendrick, E. Insights into Architecture, Design and Manufacture of Electrodes for Lithium-Ion Batteries. *Mater. Des.* **2022**, *223*, 111208. [[CrossRef](#)]
26. Etacheri, V. Sol-Gel Processed Cathode Materials for Lithium-Ion Batteries. In *Sol-Gel Materials for Energy, Environment and Electronic Applications*; Pillai, S.C., Hehir, S., Eds.; Advances in Sol-Gel Derived Materials and Technologies; Springer International Publishing: Cham, Switzerland, 2017; pp. 155–195. ISBN 978-3-319-50144-4.
27. Vertruyen, B.; Eshraghi, N.; Piffet, C.; Bodart, J.; Mahmoud, A.; Boschini, F. Spray-Drying of Electrode Materials for Lithium- and Sodium-Ion Batteries. *Materials* **2018**, *11*, 1076. [[CrossRef](#)]
28. Satyavani, T.V.S.L.; Srinivas Kumar, A.; Subba Rao, P.S.V. Methods of Synthesis and Performance Improvement of Lithium Iron Phosphate for High Rate Li-Ion Batteries: A Review. *Eng. Sci. Technol. Int. J.* **2016**, *19*, 178–188. [[CrossRef](#)]
29. Lobe, S.; Bauer, A.; Uhlenbruck, S.; Fattakhova-Rohlfing, D. Physical Vapor Deposition in Solid-State Battery Development: From Materials to Devices. *Adv. Sci.* **2021**, *8*, 2002044. [[CrossRef](#)]
30. Zhang, D.; Cai, R.; Zhou, Y.; Shao, Z.; Liao, X.-Z.; Ma, Z.-F. Effect of Milling Method and Time on the Properties and Electrochemical Performance of LiFePO₄/C Composites Prepared by Ball Milling and Thermal Treatment. *Electrochim. Acta* **2010**, *55*, 2653–2661. [[CrossRef](#)]
31. Luo, S.; Hu, D.; Liu, H.; Li, J.; Yi, T.-F. Hydrothermal Synthesis and Characterization of α -Fe₂O₃/C Using Acid-Pickled Iron Oxide Red for Li-Ion Batteries. *J. Hazard. Mater.* **2019**, *368*, 714–721. [[CrossRef](#)]
32. Choi, B.N.; Seo, J.Y.; Kim, B.; Kim, Y.S.; Chung, C.-H. Electro-Deposition of the Lithium Metal Anode on Dendritic Copper Current Collectors for Lithium Battery Application. *Appl. Surf. Sci.* **2020**, *506*, 144884. [[CrossRef](#)]
33. Zhang, J.; Huang, T.; Yu, A. Synthesis and Effect of Electrode Heat-Treatment on the Superior Lithium Storage Performance of Co₃O₄ Nanoparticles. *J. Power Sources* **2015**, *273*, 894–903. [[CrossRef](#)]
34. Ling, J.; Karuppiah, C.; Krishnan, S.G.; Reddy, M.V.; Mison, I.I.; Ab Rahim, M.H.; Yang, C.-C.; Jose, R. Phosphate Polyanion Materials as High-Voltage Lithium-Ion Battery Cathode: A Review. *Energy Fuels* **2021**, *35*, 10428–10450. [[CrossRef](#)]
35. Kim, D.-H.; Kim, J. Synthesis of LiFePO₄ Nanoparticles in Polyol Medium and Their Electrochemical Properties. *Electrochem. Solid State Lett.* **2006**, *9*, A439. [[CrossRef](#)]
36. Lai, S.Y.; Knudsen, K.D.; Sejersted, B.T.; Ulvestad, A.; Mæhlen, J.P.; Kuposov, A.Y. Silicon Nanoparticle Ensembles for Lithium-Ion Batteries Elucidated by Small-Angle Neutron Scattering. *ACS Appl. Energy Mater.* **2019**, *2*, 3220–3227. [[CrossRef](#)]
37. Fan, Y.; Zhang, N.; Zhang, L.; Shao, H.; Wang, J.; Zhang, J.; Cao, C. Co₃O₄-Coated TiO₂ Nanotube Composites Synthesized through Photo-Deposition Strategy with Enhanced Performance for Lithium-Ion Batteries. *Electrochim. Acta* **2013**, *94*, 285–293. [[CrossRef](#)]
38. Li, X.; Tian, X.; Yang, T.; Song, Y.; Liu, Y.; Guo, Q.; Liu, Z. Two-Pot Synthesis of One-Dimensional Hierarchically Porous Co₃O₄ Nanorods as Anode for Lithium-Ion Battery. *J. Alloys Compd.* **2018**, *735*, 2446–2452. [[CrossRef](#)]
39. Yin, H.; Liu, Y.; Yu, N.; Qu, H.-Q.; Liu, Z.; Jiang, R.; Li, C.; Zhu, M.-Q. Graphene-like MoS₂ Nanosheets on Carbon Fabrics as High-Performance Binder-Free Electrodes for Supercapacitors and Li-Ion Batteries. *ACS Omega* **2018**, *3*, 17466–17473. [[CrossRef](#)]
40. Chen, Z.; Wang, J.; Chao, D.; Baikie, T.; Bai, L.; Chen, S.; Zhao, Y.; Sum, T.C.; Lin, J.; Shen, Z. Hierarchical Porous LiNi_{1/3}Co_{1/3}Mn_{1/3}O₂ Nano-/Micro Spherical Cathode Material: Minimized Cation Mixing and Improved Li⁺ Mobility for Enhanced Electrochemical Performance. *Sci. Rep.* **2016**, *6*, 25771. [[CrossRef](#)]
41. Fu, W.; Wang, Y.; Kong, K.; Kim, D.; Wang, F.; Yushin, G. Materials and Processing of Lithium-Ion Battery Cathodes. *Nanoenergy Adv.* **2023**, *3*, 138–154. [[CrossRef](#)]
42. Jang, W.Y.; Reddy, C.V.; Wang, R.; Choi, J.; Son, J.; Kakarla, R.R.; Aminabhavi, T.M.; Shim, J. Synthesis of 1D/2D VO₂ (B) Nanowire/g-C₃N₄ Hybrid Architectures as Cathode Materials for High-Performance Li-Ion Batteries. *Chem. Eng. J.* **2023**, *476*, 146786. [[CrossRef](#)]
43. Bak, S.-M.; Shadika, Z.; Lin, R.; Yu, X.; Yang, X.-Q. In Situ/Operando Synchrotron-Based X-ray Techniques for Lithium-Ion Battery Research. *NPG Asia Mater.* **2018**, *10*, 563–580. [[CrossRef](#)]
44. Le Houx, J.; Kramer, D. X-ray Tomography for Lithium Ion Battery Electrode Characterisation—A Review. *Energy Rep.* **2021**, *7*, 9–14. [[CrossRef](#)]
45. Yang, M.; Bi, R.; Wang, J.; Yu, R.; Wang, D. Decoding Lithium Batteries through Advanced In Situ Characterization Techniques. *Int. J. Miner. Metall. Mater.* **2022**, *29*, 965–989. [[CrossRef](#)]
46. Pietsch, P.; Wood, V. X-ray Tomography for Lithium Ion Battery Research: A Practical Guide. *Annu. Rev. Mater. Res.* **2017**, *47*, 451–479. [[CrossRef](#)]
47. Dayani, S.; Markötter, H.; Schmidt, A.; Widjaja, M.P.; Bruno, G. Multi-Level X-ray Computed Tomography (XCT) Investigations of Commercial Lithium-Ion Batteries from Cell to Particle Level. *J. Energy Storage* **2023**, *66*, 107453. [[CrossRef](#)]
48. Dugas, R.; Forero-Saboya, J.D.; Ponrouch, A. Methods and Protocols for Reliable Electrochemical Testing in Post-Li Batteries (Na, K, Mg, and Ca). *Chem. Mater.* **2019**, *31*, 8613–8628. [[CrossRef](#)]
49. Rowden, B.; Garcia-Araez, N. Estimating Lithium-Ion Battery Behavior from Half-Cell Data. *Energy Rep.* **2021**, *7*, 97–103. [[CrossRef](#)]

50. Raccichini, R.; Amores, M.; Hinds, G. Critical Review of the Use of Reference Electrodes in Li-Ion Batteries: A Diagnostic Perspective. *Batteries* **2019**, *5*, 12. [CrossRef]
51. Minter, R.D.; Juarez-Robles, D.; Fear, C.; Barsukov, Y.; Mukherjee, P.P. Three-Electrode Coin Cell Preparation and Electrodeposition Analytics for Lithium-Ion Batteries. *J. Vis. Exp. JoVE* **2018**, *135*, 57735. [CrossRef]
52. Kodama, M.; Ohashi, A.; Adachi, H.; Miyuki, T.; Takeuchi, A.; Yasutake, M.; Uesugi, K.; Kaburagi, T.; Hirai, S. Three-Dimensional Structural Measurement and Material Identification of an All-Solid-State Lithium-Ion Battery by X-ray Nanotomography and Deep Learning. *J. Power Sources Adv.* **2021**, *8*, 100048. [CrossRef]
53. Llewellyn, A.V.; Matruglio, A.; Brett, D.J.L.; Jervis, R.; Shearing, P.R. Using In-Situ Laboratory and Synchrotron-Based X-ray Diffraction for Lithium-Ion Batteries Characterization: A Review on Recent Developments. *Condens. Matter* **2020**, *5*, 75. [CrossRef]
54. Wilson, G.; Zilinskaite, S.; Unka, S.; Boston, R.; Reeves-McLaren, N. Establishing Operando Diffraction Capability through the Study of Li-Ion (de) Intercalation in LiFePO₄. *Energy Rep.* **2020**, *6*, 174–179. [CrossRef]
55. Giorgetti, M.; Stievano, L.; Giorgetti, M.; Stievano, L. X-ray Absorption Spectroscopy Study of Battery Materials. In *X-ray Characterization of Nanostructured Energy Materials by Synchrotron Radiation*; IntechOpen: London, UK, 2017; ISBN 978-953-51-3014-7.
56. Giorgetti, M. A Review on the Structural Studies of Batteries and Host Materials by X-ray Absorption Spectroscopy. *ISRN Mater. Sci.* **2013**, *2013*, 938625. [CrossRef]
57. An, S.J.; Li, J.; Daniel, C.; Mohanty, D.; Nagpure, S.; Wood, D.L., III. The State of Understanding of the Lithium-Ion-Battery Graphite Solid Electrolyte Interphase (SEI) and Its Relationship to Formation Cycling. *Carbon* **2016**, *105*, 52–76. [CrossRef]
58. Shutthanandan, V.; Nandasiri, M.; Zheng, J.; Engelhard, M.H.; Xu, W.; Thevuthasan, S.; Murugesan, V. Applications of XPS in the Characterization of Battery Materials. *J. Electron Spectrosc. Relat. Phenom.* **2018**, *231*, 2–10. [CrossRef]
59. In Situ Chemical Imaging of Solid-Electrolyte Interphase Layer Evolution in Li-S Batteries | Chemistry of Materials. Available online: <https://pubs.acs.org/doi/10.1021/acs.chemmater.7b00374> (accessed on 27 December 2023).
60. Greczynski, G.; Hultman, L. X-ray Photoelectron Spectroscopy: Towards Reliable Binding Energy Referencing. *Prog. Mater. Sci.* **2020**, *107*, 100591. [CrossRef]
61. Spence, S.; Lee, W.-K.; Lin, F.; Xiao, X. Transmission X-ray Microscopy and Its Applications in Battery Material Research—A Short Review. *Nanotechnology* **2021**, *32*, 442003. [CrossRef]
62. Choi, P.; Parimalam, B.; Li, Y.; Litster, S. Operando Ultra-High-Resolution X-ray Microscopy of Lithium Anodes with Separator Interactions. *J. Power Sources* **2023**, *581*, 233468. [CrossRef]
63. Xu, L.; Tang, S.; Cheng, Y.; Wang, K.; Liang, J.; Liu, C.; Cao, Y.-C.; Wei, F.; Mai, L. Interfaces in Solid-State Lithium Batteries. *Joule* **2018**, *2*, 1991–2015. [CrossRef]
64. McBrayer, J.D.; Apblett, C.A.; Harrison, K.L.; Fenton, K.R.; Minter, S.D. Mechanical Studies of the Solid Electrolyte Interphase on Anodes in Lithium and Lithium Ion Batteries. *Nanotechnology* **2021**, *32*, 502005. [CrossRef]
65. Swallow, J.E.N.; Fraser, M.W.; Kneusels, N.-J.H.; Charlton, J.F.; Sole, C.G.; Phelan, C.M.E.; Björklund, E.; Bencok, P.; Escudero, C.; Pérez-Dieste, V.; et al. Revealing Solid Electrolyte Interphase Formation through Interface-Sensitive Operando X-ray Absorption Spectroscopy. *Nat. Commun.* **2022**, *13*, 6070. [CrossRef]
66. Narayanan, S.; Ulissi, U.; Gibson, J.S.; Chart, Y.A.; Weatherup, R.S.; Pasta, M. Effect of Current Density on the Solid Electrolyte Interphase Formation at the lithium|Li₆PS₅Cl Interface. *Nat. Commun.* **2022**, *13*, 7237. [CrossRef]
67. Shadik, Z.; Lee, H.; Borodin, O.; Cao, X.; Fan, X.; Wang, X.; Lin, R.; Bak, S.-M.; Ghose, S.; Xu, K.; et al. Identification of LiH and Nanocrystalline LiF in the Solid-Electrolyte Interphase of Lithium Metal Anodes. *Nat. Nanotechnol.* **2021**, *16*, 549–554. [CrossRef]
68. Guo, Y.; Wu, S.; He, Y.-B.; Kang, F.; Chen, L.; Li, H.; Yang, Q.-H. Solid-State Lithium Batteries: Safety and Prospects. *eScience* **2022**, *2*, 138–163. [CrossRef]
69. Lin, D.; Liu, Y.; Cui, Y. Reviving the Lithium Metal Anode for High-Energy Batteries. *Nat. Nanotechnol.* **2017**, *12*, 194–206. [CrossRef]
70. Steiger, J.; Kramer, D.; Mönig, R. Mechanisms of Dendritic Growth Investigated by in Situ Light Microscopy during Electrodeposition and Dissolution of Lithium. *J. Power Sources* **2014**, *261*, 112–119. [CrossRef]
71. Wood, K.N.; Kazyak, E.; Chadwick, A.F.; Chen, K.-H.; Zhang, J.-G.; Thornton, K.; Dasgupta, N.P. Dendrites and Pits: Untangling the Complex Behavior of Lithium Metal Anodes through Operando Video Microscopy. *ACS Cent. Sci.* **2016**, *2*, 790–801. [CrossRef]
72. Bai, P.; Li, J.; Brushett, F.R.; Bazant, M.Z. Transition of Lithium Growth Mechanisms in Liquid Electrolytes. *Energy Environ. Sci.* **2016**, *9*, 3221–3229. [CrossRef]
73. Wood, K.N.; Noked, M.; Dasgupta, N.P. Lithium Metal Anodes: Toward an Improved Understanding of Coupled Morphological, Electrochemical, and Mechanical Behavior. *ACS Energy Lett.* **2017**, *2*, 664–672. [CrossRef]
74. Yu, S.-H.; Huang, X.; Brock, J.D.; Abruña, H.D. Regulating Key Variables and Visualizing Lithium Dendrite Growth: An Operando X-ray Study. *J. Am. Chem. Soc.* **2019**, *141*, 8441–8449. [CrossRef]
75. Harry, K.J.; Hallinan, D.T.; Parkinson, D.Y.; MacDowell, A.A.; Balsara, N.P. Detection of Subsurface Structures underneath Dendrites Formed on Cycled Lithium Metal Electrodes. *Nat. Mater.* **2014**, *13*, 69–73. [CrossRef]
76. Cao, D.; Sun, X.; Li, Q.; Natan, A.; Xiang, P.; Zhu, H. Lithium Dendrite in All-Solid-State Batteries: Growth Mechanisms, Suppression Strategies, and Characterizations. *Matter* **2020**, *3*, 57–94. [CrossRef]
77. Chen, Y.; Yuan, X.; He, C.; Gou, Q.; Yang, N.; Xie, G.; Zhang, K.; Yao, Y.; Hou, Y. Mechanistic Exploration of Dendrite Growth and Inhibition for Lithium Metal Batteries. *Energies* **2023**, *16*, 3745. [CrossRef]

78. Lou, S.; Liu, Q.; Zhang, F.; Liu, Q.; Yu, Z.; Mu, T.; Zhao, Y.; Borovilas, J.; Chen, Y.; Ge, M.; et al. Insights into Interfacial Effect and Local Lithium-Ion Transport in Polycrystalline Cathodes of Solid-State Batteries. *Nat. Commun.* **2020**, *11*, 5700. [[CrossRef](#)]
79. Abharana, N.; Nayak, C.; Halankar, K.K.; Jha, S.N.; Bhattacharyya, D. First Results of In-Situ X-ray Absorption Spectroscopy Study on Charging–Discharging Cycles of Lithium Ion Battery at Indus-2 SRS. *Nucl. Instrum. Methods Phys. Res. Sect. Accel. Spectrometers Detect. Assoc. Equip.* **2020**, *972*, 164032. [[CrossRef](#)]
80. Kavčič, M.; Petric, M.; Rajh, A.; Isaković, K.; Vizintin, A.; Talian, S.D.; Dominko, R. Characterization of Li–S Batteries Using Laboratory Sulfur X-ray Emission Spectroscopy. *ACS Appl. Energy Mater.* **2021**, *4*, 2357–2364. [[CrossRef](#)]
81. Rahe, C.; Kelly, S.T.; Rad, M.N.; Sauer, D.U.; Mayer, J.; Figgemeier, E. Nanoscale X-ray Imaging of Ageing in Automotive Lithium Ion Battery Cells. *J. Power Sources* **2019**, *433*, 126631. [[CrossRef](#)]
82. Yao, K.P.C.; Okasinski, J.S.; Kalaga, K.; Shkrob, I.A.; Abraham, D.P. Quantifying Lithium Concentration Gradients in the Graphite Electrode of Li-Ion Cells Using Operando Energy Dispersive X-ray Diffraction. *Energy Environ. Sci.* **2019**, *12*, 656–665. [[CrossRef](#)]
83. Shi, T.; Zhang, Y.-Q.; Tu, Q.; Wang, Y.; Scott, M.C.; Ceder, G. Characterization of Mechanical Degradation in an All-Solid-State Battery Cathode. *J. Mater. Chem. A* **2020**, *8*, 17399–17404. [[CrossRef](#)]
84. Sun, N.; Liu, Q.; Cao, Y.; Lou, S.; Ge, M.; Xiao, X.; Lee, W.-K.; Gao, Y.; Yin, G.; Wang, J.; et al. Anisotropically Electrochemical–Mechanical Evolution in Solid-State Batteries and Interfacial Tailored Strategy. *Angew. Chem. Int. Ed.* **2019**, *58*, 18647–18653. [[CrossRef](#)]
85. Ebner, M.; Marone, F.; Stampanoni, M.; Wood, V. Visualization and Quantification of Electrochemical and Mechanical Degradation in Li Ion Batteries. *Science* **2013**, *342*, 716–720. [[CrossRef](#)]
86. Ziesche, R.F.; Arlt, T.; Finegan, D.P.; Heenan, T.M.M.; Tengattini, A.; Baum, D.; Kardjilov, N.; Markötter, H.; Manke, I.; Kockelmann, W.; et al. 4D Imaging of Lithium-Batteries Using Correlative Neutron and X-ray Tomography with a Virtual Unrolling Technique. *Nat. Commun.* **2020**, *11*, 777. [[CrossRef](#)]
87. Pham, M.T.M.; Darst, J.J.; Walker, W.Q.; Heenan, T.M.M.; Patel, D.; Iacoviello, F.; Rack, A.; Olbinado, M.P.; Hinds, G.; Brett, D.J.L.; et al. Prevention of Lithium-Ion Battery Thermal Runaway Using Polymer-Substrate Current Collectors. *Cell Rep. Phys. Sci.* **2021**, *2*, 100360. [[CrossRef](#)]
88. Aiello, L.; Gstrein, G.; Erker, S.; Kaltenecker, B.; Ellersdorfer, C.; Sinz, W. Optimized Nail for Penetration Test on Lithium-Ion Cells and Its Utilization for the Validation of a Multilayer Electro-Thermal Model. *Batteries* **2022**, *8*, 32. [[CrossRef](#)]
89. Magnier, L.; Lecarme, L.; Alloin, F.; Maire, E.; King, A.; Bouchet, R.; Tengattini, A.; Devaux, D. Tomography Imaging of Lithium Electrodeposits Using Neutron, Synchrotron X-ray, and Laboratory X-ray Sources: A Comparison. *Front. Energy Res.* **2021**, *9*, 657712. [[CrossRef](#)]

Disclaimer/Publisher’s Note: The statements, opinions and data contained in all publications are solely those of the individual author(s) and contributor(s) and not of MDPI and/or the editor(s). MDPI and/or the editor(s) disclaim responsibility for any injury to people or property resulting from any ideas, methods, instructions or products referred to in the content.